

## 36. Particle Detectors for Non-Accelerator Physics

Revised 2019. See various sections for authors.

36.1	Introduction . . . . .	1
36.2	High-energy cosmic-ray hadron and gamma-ray detectors . . . . .	2
36.2.1	Atmospheric fluorescence detectors . . . . .	2
36.2.2	Atmospheric Cherenkov telescopes for high-energy gamma ray astronomy . . . . .	5
36.3	Large neutrino detectors . . . . .	8
36.3.1	Deep liquid detectors for rare processes . . . . .	8
36.3.2	Neutrino telescopes . . . . .	12
36.3.3	Radio emission from (ultra-)high energy particle showers . . . . .	20
36.4	Large time-projection chambers for rare event detection . . . . .	27
36.4.1	Dark matter and other low energy signals . . . . .	28
36.4.2	$0\nu\beta\beta$ Decay . . . . .	31
36.5	Sub-Kelvin detectors . . . . .	32
36.5.1	Equilibrium thermal detectors . . . . .	33
36.5.2	Nonequilibrium Detectors . . . . .	35
36.6	Low-radioactivity background techniques . . . . .	36
36.6.1	Defining the problem . . . . .	37
36.6.2	Environmental radioactivity . . . . .	37
36.6.3	Radioactive impurities in detector and shielding components . . . . .	39
36.6.4	Radon and its progeny . . . . .	40
36.6.5	Cosmic rays . . . . .	41
36.6.6	Neutrons . . . . .	42

### 36.1 Introduction

Non-accelerator experiments have become increasingly important in particle physics. These include cosmic ray experiments (with surface, space and underground detectors), neutrino oscillation measurements with solar and atmospheric neutrinos in underground laboratories, searches for neutrino-less double beta decays and dark matter candidates again in underground laboratories, and searches for more exotic phenomena. The detectors are in the majority of the cases different from those used at accelerators. Even when the detectors are based on the same physics (e.g. tracking detectors), they are employed in radically different ways. The methods range from atmospheric scintillation detectors to massive Cherenkov detectors, from large liquid scintillator detectors to dual phase TPCs, from ultrapure ionization calorimeters to cryogenic solid state detectors. With the exception of the cosmic ray detectors, techniques for producing and testing radiologically ultra-pure materials are constantly developed. Progress is linked to pushing forward the ultra-low background frontier. In this section, some important technologies relevant for detectors on the surface and underground are discussed. Space-based detectors also use some unique instrumentation, but these are beyond the present scope of this review.

## 36.2 High-energy cosmic-ray hadron and gamma-ray detectors

### 36.2.1 Atmospheric fluorescence detectors

Revised August 2019 by L.R. Wiencke (Colorado School of Mines).

Cosmic-ray fluorescence detectors (FDs) use the atmosphere as a giant calorimeter to measure isotropic scintillation light that traces the development profiles of extensive air showers. An extensive air shower (EAS) is produced by the interactions of ultra high-energy ( $E > 10^{17}$  eV) subatomic particles in the stratosphere and upper troposphere. The amount of scintillation light generated by an EAS is proportional to the energy deposited in the atmosphere and nearly independent of the primary species. With energies extending beyond  $10^{20}$  eV these are the highest energy subatomic particles known to exist. In addition to particle arrival directions, energy spectra and primary composition, the astroparticle science investigated with FDs also includes multi-messenger studies, searches for high energy photons, neutrinos, monopoles and deeply penetrating forms of dark matter.

Previous experiments with FDs included the pioneering Fly's Eye [1,2], and the High Resolution Fly's Eye (HiRes and HiRes prototype) [3]. The current generation of experiments include the Telescope Array (TA) [4] in the northern hemisphere, and the much larger Pierre Auger Observatory (Auger) [5] in the southern hemisphere. Both are hybrid observatories. Their FD telescopes overlook sparse arrays of particle detectors on the ground. Select parameters are listed in Table 36.1. TA and Auger have each one FD site populated with additional telescopes that view up to  $60^\circ$  in elevation to measure lower EASs using a combination of scintillation and direct Cherenkov light. The Auger FD also measures UV scintillation that traces the development of atmospheric transient luminous events called "Elves" that are initiated by lightning [6]. At TA a prototype FD telescope, dubbed FAST [7], has observed EASs using wide field of view PMTs and fast timing.

**Table 36.1:** Parameters of major fluorescence detectors. Note 1: Year when all FD sites were operational. Note 2: At TA 1 of the 3 FD sites features 24 telescopes from the HiRes experiment. Note 3: A-C for one telescope where A is the full area and C the area obscured by the camera and support structures. Thus A-C is the effective light collecting area. For the modified Schmidt design at Auger, the area of the entrance pupil, A, is listed because the pupil is smaller than the mirror and thus defines the entrance aperture. For the other experiments, the area of the mirror, A, is listed

Observatory	Fly's Eye	HiRes	Telescope Array	Pierre Auger
Location	Dugway UT US	Dugway UT US	Delta UT US	Malargüe AR
Start-End	1981-1992	1996-2006	2008-present	2005-present
Sites (note 1)	2 (1986)	2 (1999)	3 (2008)	4 (2008)
Separation	3.3 km	12.6 km	31-40 km	39-62 km
Telescopes/site	67,18	21,42	12,12,14+10	6, 6, 6, 6+3
Pixel FOV	$5.5^\circ$	$1^\circ$	$1^\circ$	$1.5^\circ$
Telescope FOV	$\approx 18^\circ \times \approx 18^\circ$	$16^\circ \times 13.5^\circ$	$18^\circ \times 15^\circ$ (note 2)	$30^\circ \times 28.1^\circ$
Azi $\times$ Elv				
Light collection area (note 3)	$1.95 \text{ m}^2 - 0.25 \text{ m}^2$	$3.72 \text{ m}^2 - 0.5 \text{ m}^2$	$6.8 \text{ m}^2 - 0.85 \text{ m}^2$ (for 2 sites)	$3.80 \text{ m}^2 - 0.80 \text{ m}^2$ (modified schmidt)
Energy Scale Uncertainty	$\leq 40\%$	$\approx 20\%$	$\approx 20\%$	14%

The fluorescence light is emitted primarily between 290 and 430 nm (Figure 36.1) with major

lines at 337, 357, and 391 nm, when relativistic charged particles, primarily electrons and positrons, excite nitrogen molecules in air, resulting in transitions of the 1P and 2P systems. Reviews and references for the pioneering and recent laboratory measurements of fluorescence yield,  $Y(\lambda, P, T, u)$ , including dependence on wavelength ( $\lambda$ ), temperature ( $T$ ), pressure ( $p$ ), and humidity ( $u$ ) may be found in Refs. [8–10]. The results of various laboratory experiments have been combined (Figure 36.2) to obtain an absolute average and uncertainty for  $Y(337 \text{ nm}, 800 \text{ hPa}, 293 \text{ K}, \text{ dry air})$  of  $7.04 \pm 0.24 \text{ ph/MeV}$  after corrections for different electron beam energies and other factors. The units of ph/MeV correspond to the number of fluorescence photons produced per MeV of energy deposited in the atmosphere by the electromagnetic component of an EAS.

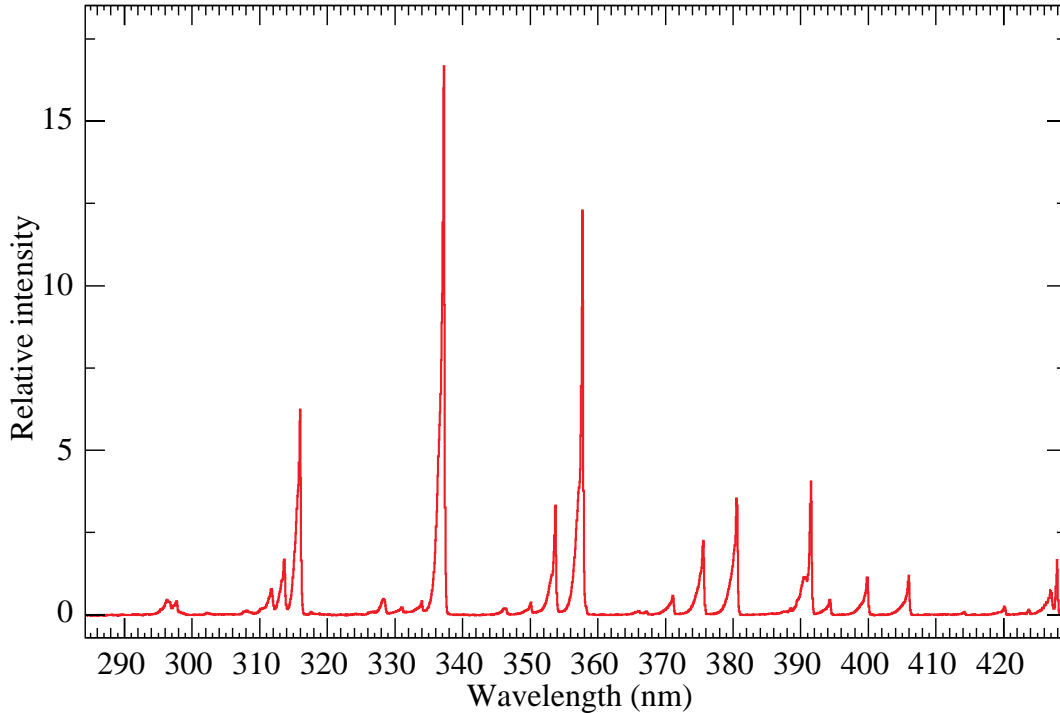


Figure 36.1: Measured fluorescence spectrum excited by 3 MeV electrons in dry air at 800 hPa and 293 K. Airfly experiment. Figure from Ref [11].

An FD element (telescope) consists of a non-tracking spherical mirror of less than astronomical quality, a close-packed “camera” of photomultiplier tubes (PMTs) near the focal plane, and a flash ADC readout system with a pulse and track-finding trigger scheme [5, 13]. The major experiments listed in Table 36.1 all use conventional PMTs (for example, Hamamatsu R9508 or Photonis XP3062) with grounded cathodes and AC coupled readout. Segmented mirrors have been fabricated from slumped or slumped/polished glass with an anodized aluminum coating or fabricated using shaped aluminum that was then chemically anodized with  $\text{AlMgSiO}_5$ . A broadband UV filter (custom fabricated or Schott MUG-6) reduces background light such as starlight, airglow, man-made light pollution, and airplane strobe-lights.

At  $10^{20} \text{ eV}$ , where the flux drops below 1 EAS/ $\text{km}^2\text{century}$ , the aperture for an eye of adjacent FD telescopes that span the horizon can reach  $10^4 \text{ km}^2 \text{ sr}$ . FD operation requires (nearly) moonless nights and clear atmospheric conditions, which imposes a duty cycle of about 10%. Arrangements of LEDs, calibrated diffuse sources [14], pulsed UV lasers [15], LIDARs <sup>1</sup> and IR detectors that

<sup>1</sup>LIDAR stands for "Light Detection and Ranging" and refers here to systems that measure atmospheric properties from the light scattered backwards from laser pulses directed into the sky.

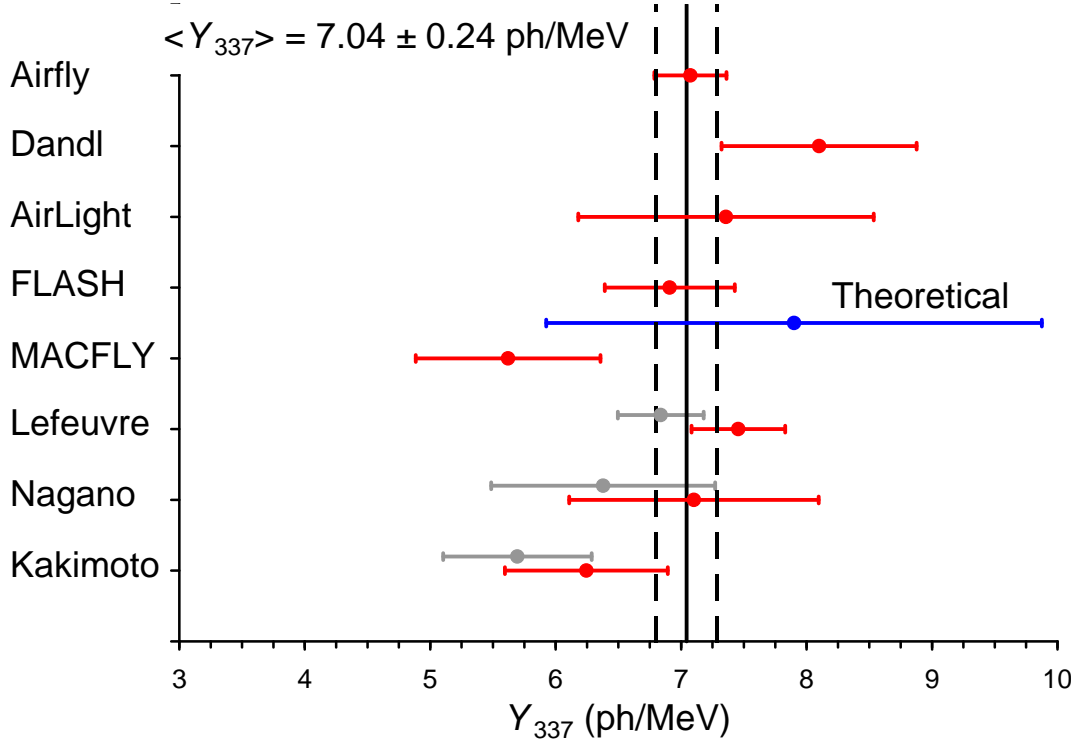


Figure 36.2: Fluorescence yield values and associated uncertainties at 337 nm ( $Y_{337}$ ) in dry air at 800 hPa and 293 K. The methodology and corrections that were applied to obtain the average and the uncertainty are discussed extensively in this reference. The vertical axis denotes different laboratory experiments that measured FY. The gray bars show three of the original measurements to illustrate the scale of the corrections applied. Figure from Ref [12].

are sensitive to clouds are used for photometric calibration, atmospheric calibration [16], and determination of exposure [17]. For purposes of optical transmission, the atmosphere is treated as having a dominant molecular component and a secondary aerosol component. The latter is well described [18] by molecular scattering theory and models derived from radiosonde measurements. The aerosol component can include dust, haze and pollution and the aerosol optical depth profile must be measured on site in the UV during FD data taking.

The EAS generates a track consistent with a light source moving at  $v = c$  across the FOV. The number of photons ( $N_\gamma$ ) as a function of atmospheric depth ( $X$ ) can be expressed as [9]

$$\frac{dN_\gamma}{dX} = \frac{dE_{\text{dep}}^{\text{tot}}}{dX} \int Y(\lambda, P, T, u) \cdot \tau_{\text{atm}}(\lambda, X) \cdot \varepsilon_{\text{FD}}(\lambda) d\lambda, \quad (36.1)$$

where  $\tau_{\text{atm}}(\lambda, X)$  is the atmospheric transmission, including wavelength ( $\lambda$ ) dependence, and  $\varepsilon_{\text{FD}}(\lambda)$  is the FD efficiency.  $\varepsilon_{\text{FD}}(\lambda)$  includes geometric factors and collection efficiency of the optics, quantum efficiency of the PMTs, and other throughput factors. The typical systematic uncertainties,  $\tau_{\text{atm}}$  (10%) and  $\varepsilon_{\text{FD}}$  (photometric calibration 10%), currently dominate the systematic uncertainty the absolute EAS energy scale. FD energy resolution, defined as event-to-event statistical uncertainty, is typically less than 10% for final data samples used for science analysis.

Analysis methods to reconstruct the EAS profile and deconvolve the contributions of re-scattered scintillation light, and direct and scattered Cherenkov light are described in [1] and more recently in [20]. The EAS energy is typically obtained by integrating over the Gaisser-Hillas function [21]

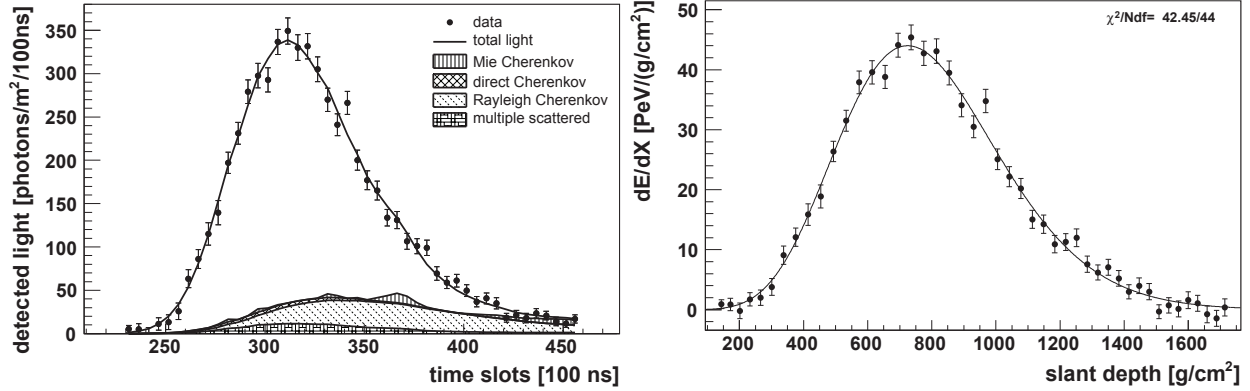


Figure 36.3: Example light profile (left) of one EAS recorded by the Pierre Auger FD and the corresponding profile (right) of energy deposited in the atmosphere vs atmospheric slant depth. The light profiles include the estimated components of Cherenkov light that have been scattered out of the forward beam by the molecular and aerosol (Mie) components of the atmosphere. The reconstructed energy of this EAS was  $3.0 \pm 0.2 \times 10^{19}$  eV. Figure from Ref [19].

$$E_{\text{cal}} = \int_0^{\infty} \left[ w_{\text{max}} \left( \frac{X - X_0}{X_{\text{max}} - X_0} \right)^{(X_{\text{max}} - X_0)/\lambda} e^{(X_{\text{max}} - X)/\lambda} \right] dX, \quad (36.2)$$

where  $E_{\text{cal}}$  is the energy of electromagnetic energy component of the EAS and  $X_{\text{max}}$  is the atmospheric slant depth at which the shower reaches its maximum energy deposit rate. This maximum  $dE/dX$  is denoted as  $w_{\text{max}}$ .  $X_0$  and  $\lambda$  are two shape parameters. The energy of the primary cosmic ray is obtained by correcting  $E_{\text{cal}}$  upward by about 10% to account for the invisible energy carried by particles that do not interact in the atmosphere. Energy resolution,  $\Delta E/E$ , of 15-20% is achievable, provided the geometric fit of the EAS axis is constrained, typically by multi-eye stereo projection or hybrid observations, and the profile fit of EAS development along the track is constrained by the observed rise and fall about  $X_{\text{max}}$ . An example of a recorded EAS light profile and its corresponding  $dE/dX$  development profile are shown in Fig. 36.3.

The EAS generates a track consistent with a light source moving at  $v = c$  across the FOV. The number of photons ( $N_\gamma$ ) as a function of atmospheric depth ( $X$ ) can be expressed as [9]

R&D toward an FD in space is at the design and prototype phase. A proposed space based FD instrument [22] by the JEM-EUSO collaboration would look down on the earth's atmosphere from space to view a much larger area than ground based instruments. Prototypes that have been built and flown include the TUS instrument [23], operated 2016-2018 onboard the Lomonosov satellite, and two FD telescopes flown on stratospheric balloons in 2014 [24] and 2017 [25]. The prototype instrument Mini-EUSO [26] (25 cm diameter aperture), currently at the International Space Station (ISS), will survey terrestrial UV emission by looking down through a UV window from inside the ISS beginning late 2019. The proposed POEMMA twin-satellite space mission [27] would record scintillation and Cherenkov light from EASs the atmosphere to measure UHECRs and PeV scale cosmogenic tau neutrinos.

### 36.2.2 Atmospheric Cherenkov telescopes for high-energy gamma ray astronomy

Revised August 2019 by J. Holder (Delaware U.; Delaware U., Bartol Inst.).

A wide variety of astrophysical objects are now known to produce high-energy  $\gamma$ -ray photons. Leptonic or hadronic particles, accelerated to relativistic energies in the source, produce  $\gamma$ -rays typically through inverse Compton boosting of ambient photons or through the decay of neutral pions

produced in hadronic interactions. At energies below  $\sim 30$  GeV,  $\gamma$ -ray emission can be efficiently detected using satellite or balloon-borne instrumentation, with an effective area approximately equal to the size of the detector (typically  $< 1$  m<sup>2</sup>). At higher energies, a technique with much larger effective collection area is desirable to measure astrophysical  $\gamma$ -ray fluxes, which decrease rapidly with increasing energy. Atmospheric Cherenkov detectors achieve effective collection areas of  $> 10^5$  m<sup>2</sup> by employing the Earth's atmosphere as an intrinsic part of the detection technique.

As described in Chapter 30, a hadronic cosmic ray or high energy  $\gamma$ -ray incident on the Earth's atmosphere triggers a particle cascade, or air shower. Relativistic charged particles in the cascade generate Cherenkov radiation, which is emitted along the shower direction, resulting in a light pool on the ground with a radius of  $\sim 130$  m. Cherenkov light is produced throughout the cascade development, with the maximum emission occurring when the number of particles in the cascade is largest, at an altitude of  $\sim 10$  km for primary energies of 100 GeV–1 TeV. Following absorption and scattering in the atmosphere, the Cherenkov light at ground level peaks at a wavelength,  $\lambda \approx 300$ –350 nm. The photon density is typically  $\sim 100$  photons/m<sup>2</sup> for a 1 TeV primary, arriving in a brief flash of a few nanoseconds duration. This Cherenkov pulse can be detected from any point within the light pool radius by using large reflecting surfaces to focus the Cherenkov light on to fast photon detectors (Fig. 36.4).

Modern atmospheric Cherenkov telescopes, such as those built and operated by the VERITAS [28], H.E.S.S. [29] and MAGIC [30] collaborations, consist of large ( $> 100$  m<sup>2</sup>) segmented mirrors on steerable altitude-azimuth mounts. A camera made from an array of photosensors is placed at the focus of each mirror and used to record a Cherenkov image of each air shower. In these imaging atmospheric Cherenkov telescopes, single-anode photomultiplier tubes (PMTs) have traditionally been used (2048, in the case of H.E.S.S. II), but silicon devices now feature in more modern designs. The telescope cameras typically cover a field-of-view of  $3 - 10^\circ$  in diameter. Images are recorded at kHz rates, the vast majority of which are due to showers with hadronic cosmic-ray primaries. The shape and orientation of the Cherenkov images are used to discriminate  $\gamma$ -ray photon events from this cosmic-ray background, and to reconstruct the photon energy and arrival direction.  $\gamma$ -ray images result from purely electromagnetic cascades and appear as narrow, elongated ellipses in the camera plane. The long axis of the ellipse corresponds to the vertical extension of the air shower, and points back towards the source position in the field-of-view. If multiple telescopes are used to view the same shower (“stereoscopy”), the source position is simply the intersection point of the various image axes. Cosmic-ray primaries produce secondaries with large transverse momenta, which initiate sub-showers. Their images are consequently wider and less regular than those with  $\gamma$ -ray primaries and, since the original charged particle has been deflected by Galactic magnetic fields before reaching the Earth, the images have no preferred orientation.

The measurable differences in Cherenkov image orientation and morphology provide the background discrimination which makes ground-based  $\gamma$ -ray astronomy possible. For point-like sources, such as distant active galactic nuclei, modern instruments can reject over 99.999% of the triggered cosmic-ray events, while retaining up to 50% of the  $\gamma$ -ray population. In the case of spatially extended sources, such as Galactic supernova remnants, the background rejection is less efficient, but the technique can be used to produce  $\gamma$ -ray maps of the emission from the source. The angular resolution depends upon the number of telescopes which view the image and the energy of the primary  $\gamma$ -ray, but is typically less than  $0.1^\circ$  per event (68% containment radius) at energies above a few hundred GeV.

The total Cherenkov yield from the air shower is proportional to the energy of the primary particle. The image intensity, combined with the reconstructed distance of the shower core from each telescope, can therefore be used to estimate the primary energy. The energy resolution of this technique, also energy-dependent, is typically 15–20% at energies above a few hundred GeV.

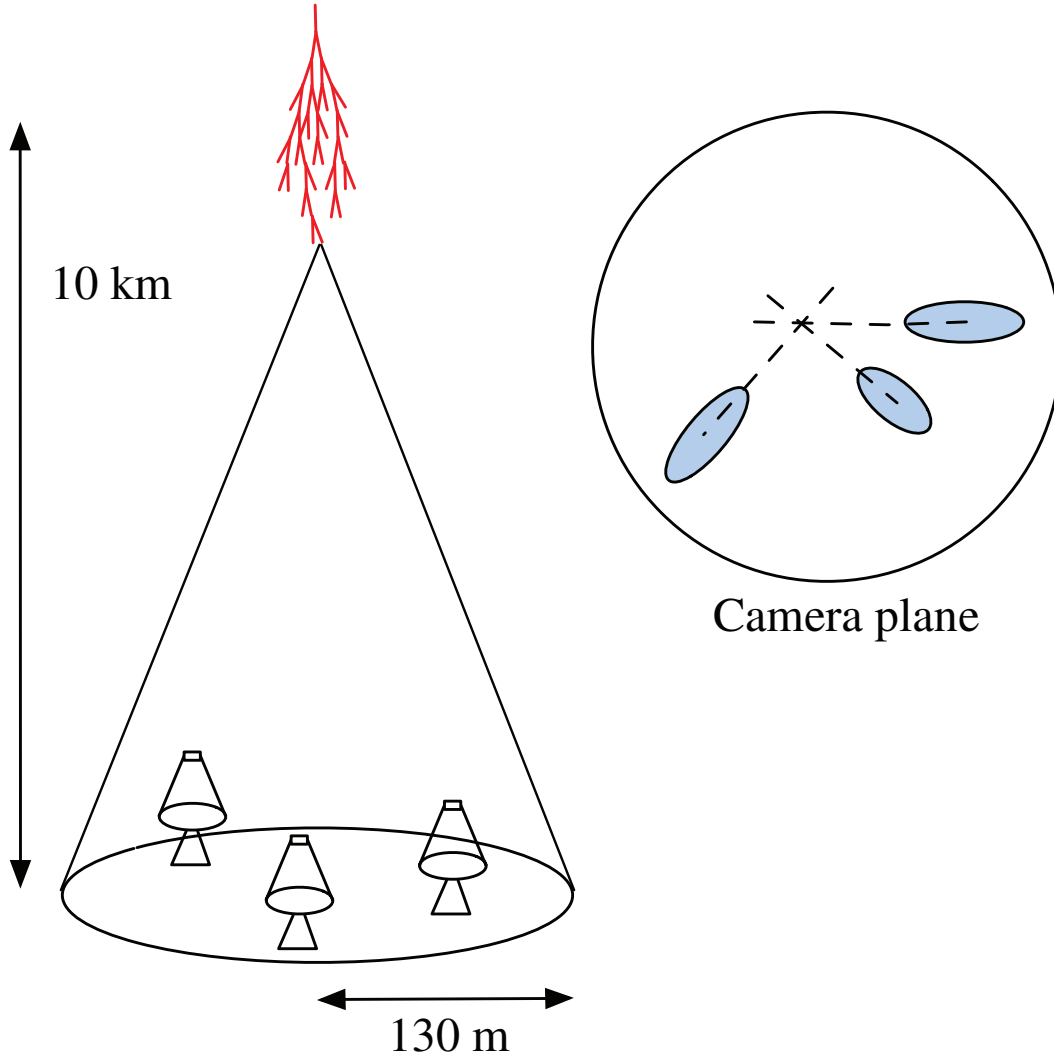


Figure 36.4: A schematic illustration of an imaging atmospheric Cherenkov telescope array. The primary particle initiates an air shower, resulting in a cone of Cherenkov radiation. Telescopes within the Cherenkov light pool record elliptical images; the intersection of the long axes of these images indicates the arrival direction of the primary, and hence the location of a  $\gamma$ -ray source in the sky

Energy spectra of  $\gamma$ -ray sources can be measured over a wide range, depending upon the instrument characteristics, source properties (flux, spectral slope, elevation angle, *etc.*), and exposure time. The effective energy range is typically from 30 GeV to 100 TeV and peak sensitivity lies in the range from 100 GeV to a few TeV.

The first astrophysical source to be convincingly detected using the imaging atmospheric Cherenkov technique was the Crab Nebula [31], with an integral flux of  $2.1 \times 10^{-11}$  photons  $\text{cm}^{-2} \text{s}^{-1}$  above 1 TeV [32]. Modern imaging atmospheric Cherenkov telescopes have sensitivity sufficient to detect sources with less than 1% of the Crab Nebula flux in a few tens of hours. The TeV source catalog now consists of over 200 sources (see e.g. Ref. [33]). A large fraction of these were detected by scanning the Galactic plane from the southern hemisphere with the H.E.S.S. telescope array [34]. Recent reviews of the field include [35] and [36], and a historical overview can be found in [37].

Major upgrades of the existing telescope arrays have recently been completed, including the addition of a 28 m diameter central telescope to H.E.S.S. (H.E.S.S. II). Development is also underway for the next generation instrument, the Cherenkov Telescope Array (CTA), which will consist of a northern and a southern hemisphere observatory, with a combined total of more than 100 telescopes [38]. Telescopes of three different sizes are planned, spread over an area of  $> 1 \text{ km}^2$ , providing wider energy coverage, improved angular and energy resolutions, and an order of magnitude improvement in sensitivity relative to existing imaging atmospheric Cherenkov telescopes. Baseline telescope designs are similar to existing devices, but exploit technological developments such as dual mirror optics and silicon photo-detectors.

### 36.3 Large neutrino detectors

#### 36.3.1 Deep liquid detectors for rare processes

Revised August 2018 by K. Scholberg (Duke U.) and C.W. Walter (Duke U.).

Deep, large detectors for rare processes tend to be multi-purpose with physics reach that includes not only solar, reactor, supernova and atmospheric neutrinos, but also searches for baryon number violation, searches for exotic particles such as magnetic monopoles, and neutrino and cosmic-ray astrophysics in different energy regimes. The detectors may also serve as targets for long-baseline neutrino beams for neutrino oscillation physics studies. In general, detector design considerations can be divided into high- and low-energy regimes, for which background and event reconstruction issues differ. The high-energy regime, from about 100 MeV to a few hundred GeV, is relevant for proton decay searches, atmospheric neutrinos and high-energy astrophysical neutrinos. The low-energy regime (a few tens of MeV or less) is relevant for supernova, solar, reactor and geological neutrinos.

Large water Cherenkov and scintillator detectors (see Table 36.2) usually consist of a volume of transparent liquid viewed by photomultiplier tubes (PMTs) (see Sec 35.2); the liquid serves as active target. PMT hit charges and times are recorded and digitized, and triggering is usually based on coincidence of PMT hits within a time window comparable to the detector's light-crossing time. Because photosensors lining an inner surface represent a driving cost that scales as surface area, very large volumes can be used for comparatively reasonable cost. Some detectors are segmented into subvolumes individually viewed by PMTs, and may include other detector elements (*e.g.*, tracking detectors). Devices to increase light collection, *e.g.*, reflectors or waveshifter plates, may be employed. A common configuration is to have at least one concentric outer layer of liquid material separated from the inner part of the detector to serve as shielding against ambient background. If optically separated and instrumented with PMTs, an outer layer may also serve as an active veto against entering cosmic rays and other background events. The PMTs for large detectors typically range in size from 20 cm to 51 cm diameter, and typical quantum efficiencies are in the 20–25% range for scintillation and water-Cherenkov photons. PMTs with higher quantum efficiencies, 35% or higher, have recently become available. The active liquid volume requires purification and there may be continuous recirculation of liquid. For large homogeneous detectors, the event interaction vertex is determined using relative timing of PMT hits, and energy deposition is determined from the number of recorded photoelectrons. A “fiducial volume” is usually defined within the full detector volume, some distance away from the PMT array. Inside the fiducial volume, enough PMTs are illuminated per event that reconstruction is considered reliable, and furthermore, entering background from the enclosing walls is suppressed by a buffer of self-shielding. PMT and detector optical parameters are calibrated using laser, LED, or other light sources. Quality of event reconstruction typically depends on photoelectron yield, pixelization and timing.

Because in most cases one is searching for rare events, large detectors are usually sited under-

**Table 36.2:** Properties of large detectors for rare processes. If total target mass is divided into large submodules, the number of subdetectors is indicated in parentheses. Projects with first data expected in 2021 or later are indicated in italics.

Detector	Mass, kton (modules)	PMTs (diameter, cm)	$\xi$	p.e./MeV	Dates
Baksan	0.33, scint (3150)	1/module (15)	segmented	40	1980–
MACRO	0.56, scint (476)	2-4/module (20)	segmented	18	1989–2000
LVD	1, scint. (840)	3/module (15)	segmented	15	1992–
KamLAND	0.41*, scint	1325(43)+554(51) <sup>†</sup>	34%	460	2002–
Borexino	0.1*, scint	2212 (20)	30%	500	2007–
SNO+	0.78, scint <sup>‡</sup>	9394 (20)	47%	400–600	2019 (exp.)
CHOOZ	0.005, scint (Gd)	192 (20)	15%	130	1997–1998
Double Chooz	0.017, scint (Gd)(2)	534/module (20)	13%	180	2011–
Daya Bay	0.160, scint (Gd)(8)	192/module (20)	5.6% <sup>§</sup>	100	2011–
RENO	0.032, scint (Gd)(2)	342/module (25)	12.6%	100	2011–
<i>JUNO</i>	20.0*, scint	17613 (51)/25600 (8)	77.9%	1200	2021 (exp.)
IMB-1	3.3*, H <sub>2</sub> O	2048 (12.5)	1%	0.25	1982–1985
IMB-2	3.3*, H <sub>2</sub> O	2048 (20)	4.5%	1.1	1987–1990
Kam I	0.88/0.78*, H <sub>2</sub> O	1000/948 (51)	20%	3.4	1983–1985
Kam II	1.04*, H <sub>2</sub> O	948 (51)	20%	3.4	1986–1990
Kam III	1.04*, H <sub>2</sub> O	948 (51)	20% <sup>¶</sup>	4.3	1990–1995
SK I	22.5*, H <sub>2</sub> O	11146 (51)	40%	6	1996–2001
SK II	22.5*, H <sub>2</sub> O	5182 (51)	19%	3	2002–2005
SK III-V	22.5*, H <sub>2</sub> O	11129 (51)	40%	6	2006–
SK-Gd	22.5*, H <sub>2</sub> O (Gd)	11129 (51)	40%	6	2020 (exp.)
<i>Hyper-K</i>	187*, H <sub>2</sub> O <sup>  </sup>	40000 (51)	40%	12	2027 (exp.)
SNO	1, D <sub>2</sub> O/1.7, H <sub>2</sub> O	9438 (20)	31% <sup>**</sup>	9	1999–2006

\*Indicates typical fiducial mass used for data analysis; this may vary by physics topic.

<sup>†</sup>Measurements made before 2003 only considered data from the 43 cm PMTs.

<sup>‡</sup>SNO+ ran with water fill from May 2017 to July 2019.

<sup>§</sup>The effective Daya Bay coverage is 12% with top and bottom reflectors.

<sup>¶</sup>The effective Kamiokande III coverage was 25% with light collectors.

<sup>||</sup>A second staged module is planned.

<sup>\*\*</sup>The effective SNO coverage was 54% with light collectors.

ground to reduce cosmic-ray-related background (see Chapter 30). The minimum depth required varies according to the physics goals [39].

### 36.3.1.1 Liquid scintillator detectors

Past and current large underground detectors based on hydrocarbon scintillators include LVD, MACRO, Baksan, Borexino, KamLAND and SNO+; JUNO is a future detector. Experiments at nuclear reactors include CHOOZ, Double CHOOZ, Daya Bay, and RENO. Organic liquid scintillators (see Section 35.3) for large detectors are chosen for high light yield and attenuation length, good stability, compatibility with other detector materials, high flash point, low toxicity, appropriate density for mechanical stability, and low cost. They may be doped with waveshifters and stabilizing agents. Popular choices are pseudocumene (1,2,4-trimethylbenzene) with a few g/L of the PPO (2,5-diphenyloxazole) fluor, and linear alkylbenzene (LAB). In a typical detector configu-

ration there will be active or passive regions of undoped scintillator, non-scintillating mineral oil or water surrounding the inner neutrino target volume. A thin vessel or balloon made of nylon, acrylic or other material transparent to scintillation light may contain the inner target; if the scintillator is buoyant with respect to its buffer, ropes may hold the balloon in place. For phototube surface coverages in the 20–40% range, yields in the few hundreds of photoelectrons per MeV of energy deposition can be obtained. Typical energy resolution is about  $7\%/\sqrt{E(\text{MeV})}$ , and typical position reconstruction resolution is a few tens of cm at  $\sim 1$  MeV, scaling as  $\sim N^{-1/2}$ , where  $N$  is the number of photoelectrons detected.

Shallow detectors for reactor neutrino oscillation experiments require excellent muon veto capabilities. For  $\bar{\nu}_e$  detection via inverse beta decay on free protons,  $\bar{\nu}_e + p \rightarrow n + e^+$ , the neutron is captured by a proton on a  $\sim 180 \mu\text{s}$  timescale, resulting in a 2.2 MeV  $\gamma$  ray, observable by Compton scattering and which can be used as a tag in coincidence with the positron signal. The positron annihilation  $\gamma$  rays may also contribute. Inverse beta decay tagging may be improved by addition of Gd at  $\sim 0.1\%$  by mass, which for natural isotope abundance has a  $\sim 49,000$  barn cross-section for neutron capture (in contrast to the 0.3 barn cross-section for capture on free protons). Gd capture takes  $\sim 30 \mu\text{s}$ , and is followed by a cascade of  $\gamma$  rays adding up to about 8 MeV. Gadolinium doping of scintillator requires specialized formulation to ensure adequate attenuation length and stability.

Scintillation detectors have an advantage over water Cherenkov detectors in the lack of Cherenkov threshold and the high light yield. However, scintillation light emission is nearly isotropic, and therefore directional capabilities are relatively weak. Liquid scintillator is especially suitable for detection of low-energy events. Radioactive backgrounds are a serious issue, and include long-lived cosmogenics. To go below a few MeV, very careful selection of materials and purification of the scintillator is required (see Section 36.6). Fiducialization and tagging can reduce background. One can also dissolve neutrinoless double beta decay ( $0\nu\beta\beta$ ) isotopes in scintillator. This has been realized by KamLAND-Zen, which deployed a 1.5 m-radius balloon containing enriched Xe dissolved in scintillator inside KamLAND, and  $^{130}\text{Te}$  is planned for SNO+. Although for this approach, energy resolution is poor compared to other  $0\nu\beta\beta$  search experiments, the quantity of isotope can be so large that the kinematic signature of  $0\nu\beta\beta$  would be visible as a clear feature in the spectrum.

### 36.3.1.2 Water Cherenkov detectors

Very large imaging water detectors reconstruct ten-meter-scale Cherenkov rings produced by charged particles (see Section 35.5). The first such large detectors were IMB and Kamiokande. The only currently existing instance of this class of detector, with fiducial mass of 22.5 kton and total mass of 50 kton, is Super-Kamiokande (Super-K, SK). Hyper-Kamiokande (Hyper-K) plans at least one, and possibly two, detectors with 187-kton fiducial mass. For volumes of this scale, absorption and scattering of Cherenkov light are non-negligible, and a wavelength-dependent factor  $\exp(-d/L(\lambda))$  (where  $d$  is the distance from emission to the sensor and  $L(\lambda)$  is the attenuation length of the medium) must be included in the integral of Eq. (35.6) for the photoelectron yield. Attenuation lengths on the order of 100 meters have been achieved.

Cherenkov detectors are excellent electromagnetic calorimeters, and the number of Cherenkov photons produced by an  $e/\gamma$  is nearly proportional to its kinetic energy. For massive particles, the number of photons produced is also related to the energy, but not linearly. For any type of particle, the *visible energy*  $E_{\text{vis}}$  is defined as the energy of an electron which would produce the same number of Cherenkov photons. The number of collected photoelectrons depends on the scattering and attenuation in the water along with the photo-cathode coverage, quantum efficiency and the optical parameters of any external light collection systems or protective material surrounding them. Event-by-event corrections are made for geometry and attenuation. For a typical case, in water  $N_{\text{p.e.}} \sim 15 \xi E_{\text{vis}}(\text{MeV})$ , where  $\xi$  is the effective fractional photosensor coverage. Cherenkov

photoelectron yield per MeV of energy is relatively small compared to that for scintillator, *e.g.*,  $\sim 6$  pe/MeV for Super-K with a PMT surface coverage of  $\sim 40\%$ . In spite of light yield and Cherenkov threshold issues, the intrinsic directionality of Cherenkov light allows individual particle tracks to be reconstructed. Vertex and direction fits are performed using PMT hit charges and times, requiring that the hit pattern be consistent with a Cherenkov ring.

High-energy ( $\sim 100$  MeV or more) neutrinos from the atmosphere or beams interact with nucleons; for the nucleons bound inside the  $^{16}\text{O}$  nucleus, nuclear effects must be considered both at the interaction and as the particles leave the nucleus. Various event topologies can be distinguished by their timing and fit patterns, and by presence or absence of light in a veto. “Fully-contained” events are those for which the neutrino interaction final state particles do not leave the inner part of the detector; these have their energies relatively well measured. Neutrino interactions for which the lepton is not contained in the inner detector sample have higher-energy parent neutrino energy distributions. For example, in “partially-contained” events, the neutrino interacts inside the inner part of the detector but the lepton (almost always a muon, since only muons are penetrating) exits. “Upward-going muons” can arise from neutrinos which interact in the rock below the detector and create muons which enter the detector and either stop, or go all the way through (entering downward-going muons cannot be distinguished from cosmic rays). At high energies, multi-photoelectron hits are likely and the charge collected by each PMT (rather than the number of PMTs firing) must be used; this degrades the energy resolution to approximately  $2\%/\sqrt{\xi E_{\text{vis}}(\text{GeV})}$ . The absolute energy scale in this regime can be known to  $\sim 2\text{--}3\%$  using cosmic-ray muon energy deposition, Michel electrons and  $\pi^0$  from atmospheric neutrino interactions. Typical vertex resolutions for GeV energies are a few tens of cm [40]. Angular resolution for determination of the direction of a charged particle track is a few degrees. For a neutrino interaction, because some final-state particles are usually below Cherenkov threshold, knowledge of direction of the incoming neutrino direction itself is generally worse than that of the lepton direction, and dependent on neutrino energy.

Multiple particles in an interaction (so long as they are above Cherenkov threshold) may be reconstructed, allowing for the exclusive reconstruction of final states. In searches for proton decay, multiple particles can be kinematically reconstructed to form a decaying nucleon. High-quality particle identification is also possible:  $\gamma$  rays and electrons shower, and electrons scatter, which results in fuzzy rings, whereas muons, pions and protons make sharp rings. These patterns can be quantitatively separated with high reliability using maximum likelihood methods [41]. A  $e/\mu$  misidentification probability of  $\sim 0.4\%/\xi$  in the sub-GeV range is consistent with the performance of several experiments for  $4\% < \xi < 40\%$ . Sources of background for high energy interactions include misidentified cosmic muons and anomalous light patterns when the PMTs sometimes “flash” and emit photons themselves. The latter class of events can be removed using its distinctive PMT signal patterns, which may be repeated. More information about high energy event selection and reconstruction may be found in reference [42].

In spite of the fairly low light yield, large water Cherenkov detectors may be employed for reconstructing low-energy events, down to *e.g.*  $\sim 4\text{--}5$  MeV for Super-K [43]. Low-energy neutrino interactions of solar neutrinos in water are predominantly elastic scattering off atomic electrons; single electron events are then reconstructed. At solar neutrino energies, the visible energy resolution ( $\sim 30\%/\sqrt{\xi E_{\text{vis}}(\text{MeV})}$ ) is about 20% worse than photoelectron counting statistics would imply. Using an electron LINAC and/or nuclear sources, approximately 0.5% determination of the absolute energy scale has been achieved at solar neutrino energies. Angular resolution is limited by multiple scattering in this energy regime ( $25\text{--}30^\circ$ ). At these energies, radioactive backgrounds become a dominant issue. These backgrounds include radon in the water itself or emanated from detector materials, and  $\gamma$  rays from the rock and detector materials. In the few to few tens of

MeV range, radioactive products of cosmic-ray-muon-induced spallation are troublesome, and are removed by proximity in time and space to preceding muons, at some cost in dead time. Gadolinium doping using 0.2%  $\text{Gd}_2(\text{SO}_4)_3$  is planned for Super-K to improve selection of low-energy  $\bar{\nu}_e$  and other events with accompanying neutrons [44].

The Sudbury Neutrino Observatory (SNO) detector [45] is the only instance of a large heavy water detector and deserves mention here. In addition to an outer 1.7 kton of light water, SNO contained 1 kton of  $\text{D}_2\text{O}$ , giving it unique sensitivity to neutrino neutral current ( $\nu_x + d \rightarrow \nu_x + p + n$ ), and charged current ( $\nu_e + d \rightarrow p + p + e^-$ ) deuteron breakup reactions. The neutrons were detected in three ways: In the first phase, via the reaction  $n + d \rightarrow t + \gamma + 6.25$  MeV; Cherenkov radiation from electrons Compton-scattered by the  $\gamma$  rays was observed. In the second phase, NaCl was dissolved in the water.  $^{35}\text{Cl}$  captures neutrons,  $n + ^{35}\text{Cl} \rightarrow ^{36}\text{Cl} + \gamma + 8.6$  MeV. The  $\gamma$  rays were observed via Compton scattering. In a final phase, specialized low-background  $^3\text{He}$  counters (“neutral current detectors” or NCDs) were deployed in the detector. These counters detected neutrons via  $n + ^3\text{He} \rightarrow p + t + 0.76$  MeV; ionization charge from energy loss of the products was recorded in proportional counters.

### 36.3.2 Neutrino telescopes

Revised August 2019 by U.F. Katz (Erlangen U.) and C. Spiering (DESY, Zeuten).

The primary goal of neutrino telescopes (NTs) is the detection of astrophysical neutrinos, in particular those which are expected to accompany the production of high-energy cosmic rays in astrophysical accelerators. NTs in addition address a variety of other fundamental physics issues like indirect search for dark matter, study of neutrino oscillations, search for exotic particles like magnetic monopoles or study of cosmic rays and their interactions [46–48]. Electromagnetic radio frequency detectors for high energy neutrinos are discussed in "Radio emission from (ultra-) high energy particle showers" section 36.3.3.

NTs are large-volume arrays of “optical modules” (OMs) installed in open transparent media like water or ice, at depths that completely block the daylight. The OMs record the Cherenkov light induced by charged secondary particles produced in reactions of high-energy neutrinos in or around the instrumented volume. The neutrino energy,  $E_\nu$ , and direction can be reconstructed from the hit pattern recorded. NTs typically target an energy range  $E_\nu \gtrsim 100$  GeV; sensitivity to lower energies is achieved in dedicated setups with denser instrumentation.

In detecting cosmic neutrinos, three sources of backgrounds have to be considered: (i) *atmospheric neutrinos* from cosmic-ray interactions in the atmosphere, which can be separated from cosmic neutrinos on a statistical basis, or, for down-going neutrinos, by vetoing accompanying muons; (ii) down-going punch-through *atmospheric muons* from cosmic-ray interactions, which are suppressed by several orders of magnitude with respect to the ground level due to the large detector depths. They can be further reduced by selecting upward-going or high-energy neutrinos or by self-veto methods; (iii) random backgrounds due to photomultiplier (PMT) dark counts,  $^{40}\text{K}$  decays (mainly in sea water) or bioluminescence (only water), which impact adversely on event recognition and reconstruction. Note that atmospheric neutrinos and muons allow for investigating neutrino oscillations and cosmic ray anisotropies, respectively.

Recently, it has become obvious that a precise measurement of the energy-zenith-distribution of atmospheric neutrinos may allow for determining the neutrino mass hierarchy by exploiting matter-induced oscillation effects in the Earth [49, 50].

Neutrinos can interact with target nucleons  $N$  through charged current ( $\vec{\nu}_\ell N \rightarrow \ell^\mp X$ , CC) or neutral current ( $\vec{\nu}_\ell N \rightarrow \vec{\nu}_\ell X$ , NC) processes. A CC reaction of a  $\vec{\nu}_\mu$  produces a muon track and a hadronic particle cascade, whereas all NC reactions and CC reactions of  $\vec{\nu}_e$  produce particle cascades only. CC interactions of  $\vec{\nu}_\tau$  can have either signature, depending on the  $\tau$  decay mode.

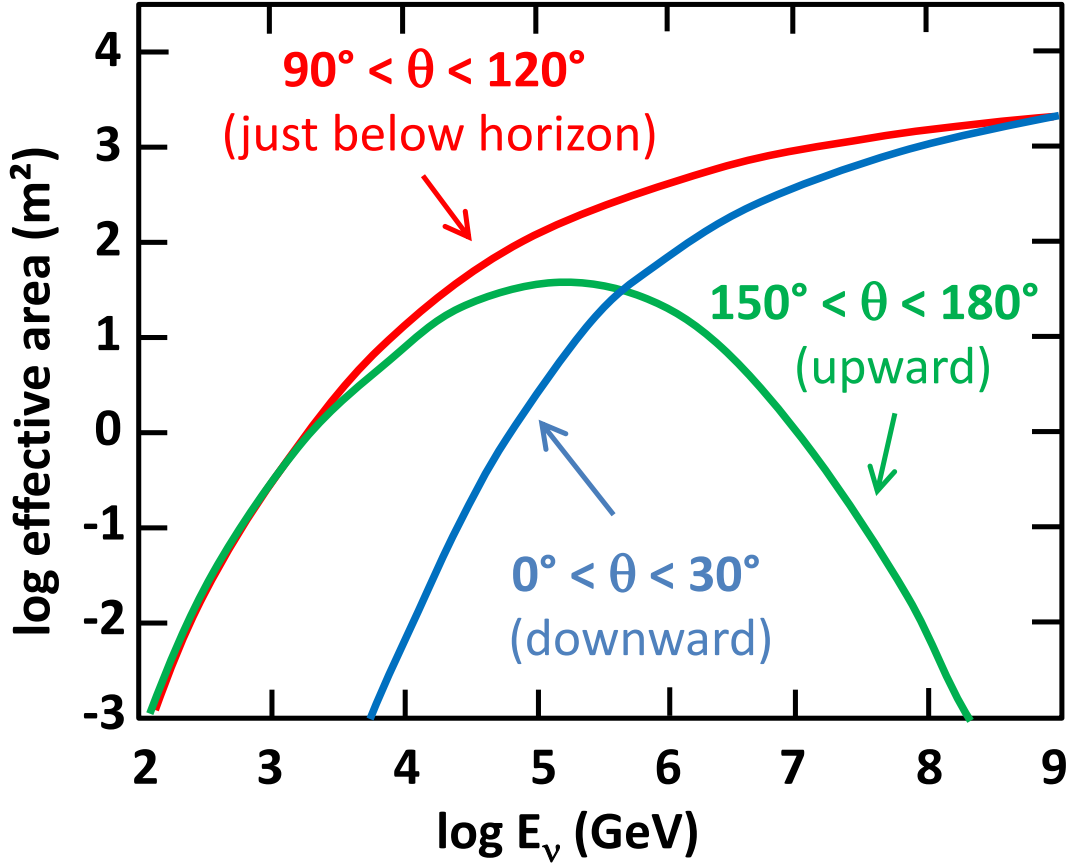


Figure 36.5: Effective  $\bar{\nu}_\mu$  area for IceCube as an example of a cubic-kilometre NT, as a function of neutrino energy for three intervals of the zenith angle  $\theta$ . The values shown here correspond to a specific event selection for point source searches.

In most astrophysical models, neutrinos are expected to be produced through the  $\pi/K \rightarrow \mu \rightarrow e$  decay chain, *i.e.*, with a flavour ratio  $\nu_e : \nu_\mu : \nu_\tau \approx 1 : 2 : 0$ . For sources outside the solar system, neutrino oscillations turn this ratio to  $\nu_e : \nu_\mu : \nu_\tau \approx 1 : 1 : 1$  upon arrival on Earth.

The total neutrino-nucleon cross section is about  $10^{-35} \text{ cm}^2$  at  $E_\nu = 1 \text{ TeV}$  and rises roughly linearly with  $E_\nu$  below this energy and as  $E_\nu^{0.3-0.5}$  above, flattening out towards high energies. The CC:NC cross-section ratio is about 2:1. At energies above some TeV, neutrino absorption in the Earth becomes noticeable; for vertically upward-moving neutrinos (zenith angle  $\theta = 180^\circ$ ), the survival probability is 74 (27, < 2)% for 10 (100, 1000) TeV. On average, between 50% (65%) and 75% of  $E_\nu$  is transferred to the final-state lepton in neutrino (antineutrino) reactions between 100 GeV and 10 PeV.

The final-state lepton follows the initial neutrino direction with a RMS mismatch angle  $\langle \phi_{\nu\ell} \rangle \approx 1.5^\circ / \sqrt{E_\nu [\text{TeV}]}$ , indicating the intrinsic kinematic limit to the angular resolution of NTs. For CC  $\bar{\nu}_\mu$  reactions at energies above about 10 TeV, the angular resolution is dominated by the muon reconstruction accuracy of a few times  $0.1^\circ$  at most. For muon energies  $E_\mu \gtrsim 1 \text{ TeV}$ , the increasing light emission due to radiative processes allows for reconstructing  $E_\mu$  from the measured  $dE_\mu/dx$  with an accuracy of  $\sigma(\log E_\mu) \approx 0.3$ ; at lower energies,  $E_\mu$  can be estimated from the length of the muon track if it is contained in the detector. These properties make CC  $\bar{\nu}_\mu$  reactions the prime channel for the identification of individual astrophysical neutrino sources.

Hadronic and electromagnetic particle cascades at the relevant energies are 5–20 m long, *i.e.*, short compared to typical OM distances. The total amount of Cherenkov light provides a direct measurement of the cascade energy with an accuracy of about 20% at energies above 10 TeV and 10% beyond 100 TeV for events contained in the instrumented volume. Neutrino flavour and reaction mechanism can, however, hardly be determined and neutrinos from NC reactions or  $\tau$  decays may carry away significant “invisible” energy. Above 100 TeV, the average directional reconstruction accuracy of cascades is 10–15 degrees in polar ice and better than 2 degrees in water, the difference being due to the inhomogeneity of the ice and stronger light scattering in ice. These features, together with the small background of atmospheric  $\vec{\nu}_e$  and  $\vec{\nu}_\tau$  events, makes the cascade channel particularly interesting for searches for a diffuse, high-energy excess of extraterrestrial over atmospheric neutrinos. In water, cascade events can also be used for the search for point sources of cosmic neutrinos, albeit the inferior angular accuracy compared to muon tracks leads to a higher background from atmospheric neutrinos.

The detection efficiency of a NT is quantified by its effective area, *e.g.*, the fictitious area for which the full incoming neutrino flux would be recorded (see Figure 36.5). The increase with  $E_\nu$  is due to the rise of neutrino cross section and muon range, while neutrino absorption in the Earth causes the decrease at large  $\theta$ . Identification of downward-going neutrinos requires strong cuts against atmospheric muons, hence the cut-off towards low  $E_\nu$ . Due to the small cross section, the effective area is many orders of magnitude smaller than the geometrical dimension of the detector; a  $\vec{\nu}_\mu$  with 1 TeV can, *e.g.*, be detected with a probability of the order  $10^{-6}$  if the NT is on its path.

Detection of upward-going muons allows for identifying neutrino interactions far outside the instrumented volume. This method, however, is only sensitive to CC  $\vec{\nu}_\mu$  interactions and cannot be extended to more than 5–10 degrees above the geometric horizon, where the background of atmospheric muons becomes prohibitive. Alternatively, one can select events that start inside the instrumented volume and thus remove incoming muons that generate early hits in the outer layers of the detector. Such a veto-based event selection is sensitive to neutrinos of all flavours from all directions, albeit with a reduced efficiency since a part of the instrumented volume is sacrificed for the veto. Such a muon veto, or vetoing events with a coincident signal in the surface array, also rejects down-going atmospheric neutrinos that are accompanied by muons from the same air shower and thus reduces the atmospheric-neutrino background. Actually, the breakthrough in detecting high-energy cosmic neutrinos has been achieved with this technique.

Note that the fields of view of NTs at the South Pole and in the Northern hemisphere are complementary for each reaction channel and neutrino energy.

### 36.3.2.1 The Projects

Table 36.3 lists past, present and future neutrino telescope projects and their main parameters.

### 36.3.2.2 Properties of media

The efficiency and quality of event reconstruction depend strongly on the optical properties (absorption and scattering length, intrinsic optical activity) of the medium in the spectral range of bialkali photocathodes (300–550 nm). Large absorption lengths result in a better light collection, large scattering lengths in superior angular resolution. Deep-sea sites typically have effective scattering lengths of  $> 100$  m and, at their peak transparency around 450 nm, absorption lengths of 50–65 m. The absorption length for Lake Baikal is 22–24 m. The properties of South Polar ice vary strongly with depth; at the peak transparency wave length (400 nm), the scattering length is between 5 and 75 m and the absorption length between 15 and 250 m, with the best values in the depth region 2200–2450 m and the worst ones in the layer 1950–2100 m.

Noise rates measured by 25 cm PMTs in deep polar ice are about 0.5 kHz per PMT and almost entirely due to radioactivity in the OM components. The corresponding rates in sea water are

**Table 36.3:** Past, present and future NT projects and their main parameters. The milestone years give the times of project start, of first data taking with partial configurations, of detector completion, and of project termination. Projects with first data expected past 2020 are indicated in italics. The size refers to the largest instrumented volume reached during the project development. See [48] for references to the different projects where unspecified.

Experiment	Milestones	Location	Size (km <sup>3</sup> )	Remarks
DUMAND	1978/-/-/1995	Pacific Ocean		Terminated due to technical/funding problems
NT-200	1980/1993/1998/2015	Lake Baikal	10 <sup>-4</sup>	First proof of principle
GVD [51]	2012/2015/-/-	Lake Baikal	0.5–1.5	High-energy $\nu$ astronomy first 5 clusters installed
NESTOR	1991/-/-/-	Med. Sea		2004 data taking with prototype
NEMO	1998/-/-/-	Med. Sea		R&D project, prototype tests
AMANDA	1990/1996/2000/2009	South Pole	0.015	First deep-ice NT
ANTARES	1997/2006/2008/-	Med. Sea	0.010	First deep-sea NT
IceCube	2001/2005/2010/-	South Pole	1.0	First km <sup>3</sup> -sized detector
<i>IceCube-Gen2</i> [52]	2014/-/-/-	South Pole	5–10	Planned extension of IceCube covering low and high energies, a surface array and radio detection
KM3NeT/ARCA [50]	2013/(2015)/-/-	Med. Sea	ca. 1	First construction phase started
KM3NeT/ORCA [50]	2014/(2017)/-/-	Med. Sea	0.003	Low-energy configuration for neutrino mass hierarchy
<i>KM3NeT Phase 3</i>	2013/-/-/-	Med. Sea	ca. 3	6 ARCA blocks + ORCA

typically 60 kHz, mostly due to <sup>40</sup>K decays. Bioluminescence activity can locally cause rates on the MHz scale for seconds; the frequency and intensity of such “bursts” depends strongly on the sea current, the season, the geographic location, and the detector geometry. Experience from ANTARES shows that these backgrounds are manageable without a major loss of efficiency or experimental resolution.

### 36.3.2.3 Technical realisation

Optical modules (OMs) and PMTs: An OM is a pressure-tight glass sphere housing one or several PMTs with a time resolution in the nanosecond range, and in most cases also electronics for control, HV generation, operation of calibration LEDs, time synchronisation and signal digitisation.

Hybrid PMTs with 37 cm diameter have been used for NT-200, conventional hemispheric PMTs for AMANDA (20 cm) and for ANTARES, IceCube and Baikal-GVD (25 cm). A novel concept has been chosen for KM3NeT. The OMs (43 cm) are equipped with 31 PMTs (7.5 cm), plus control, calibration and digitisation electronics. The main advantages are that (i) the overall photocathode area exceeds that of a 25 cm PMT by more than a factor of 3; (ii) the individual readout of the PMTs results in a very good separation between one- and two-photoelectron signals which is essential for online data filtering and random background suppression; (iii) the hit pattern on an OM provides directional information; (iv) no mu-metal shielding against the Earth magnetic field is required. Figure 36.6 shows the OM designs of IceCube and KM3NeT.

Readout and data filtering: In current NTs the PMT data are digitised in situ, for ANTARES and Baikal-GVD in special electronics containers close to the OMs, for IceCube and KM3NeT inside

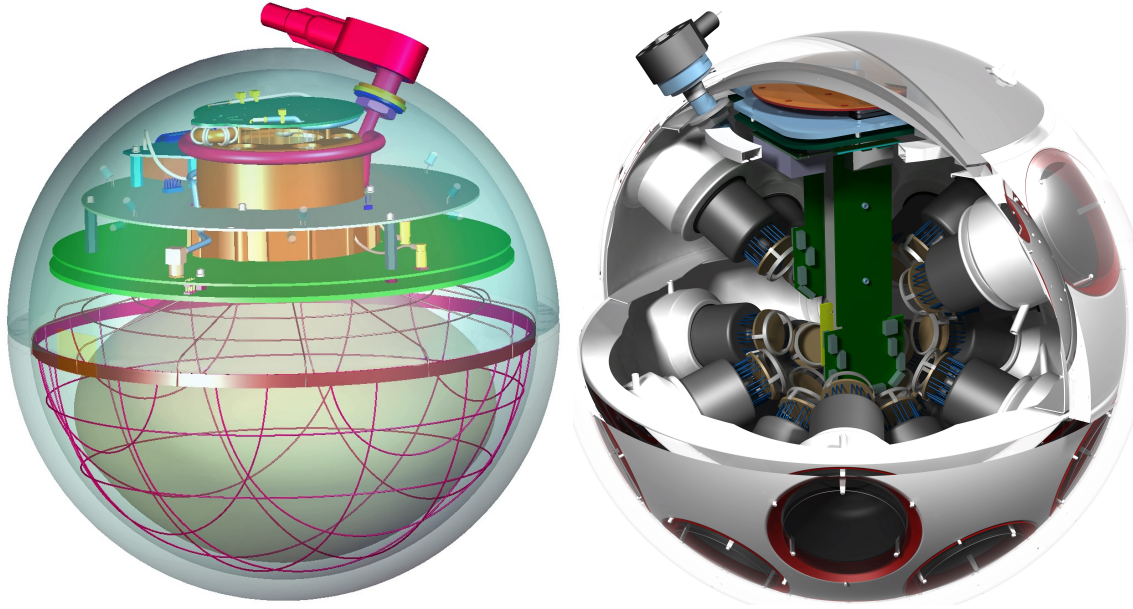


Figure 36.6: Schematic views of the digital OMs of IceCube (left) and KM3NeT (right).

the OMs. For IceCube, data are transmitted via electrical cables of up to 3.3 km length, depending on the location of the strings and the depth of the OMs; for ANTARES, KM3NeT and Baikal-GVD optical fibre connections have been chosen (several 10 km for the first two and 4 km for GVD).

The full digitised waveforms of the IceCube OMs are transmitted to the surface for pulses appearing in local coincidences on a string; for other pulses, only time and charge information is provided. For ANTARES (time and charge) and KM3NeT (time over threshold), all PMT signals above an adjustable noise threshold are sent to shore.

The raw data are subsequently processed on online computer farms, where multiplicity and topology-driven filter algorithms are applied to select event candidates. The filter output data rate is about 10 GByte/day for ANTARES and of the order 1 TByte/day for IceCube (100 GByte/day transferred via satellite) and KM3NeT.

Calibration: For efficient event recognition and reconstruction, the OM timing must be synchronised at the few-nanosecond level and the OM positions and orientations must be known to a few 10 cm and a few degrees, respectively. Time calibration is achieved by sending time synchronisation signals to the OM electronics and also by light calibration signals emitted in situ at known times by LED or laser flashers (ANTARES, KM3NeT). Precise position calibration is achieved by measuring the travel time of light calibration signals sent from OM to OM (IceCube) or acoustic signals sent from transducers at the sea floor to receivers on the detector strings (ANTARES, KM3NeT, Baikal-GVD). Absolute pointing and angular resolution can be determined by measuring the “shadow of the moon” (*i.e.*, the directional depletion of muons generated in cosmic-ray interactions). IceCube has shown that both are below  $1^\circ$ , confirming MC calculations which indicate a precision of  $\approx 0.5^\circ$  for energies above 10 TeV. For KM3NeT, simulations indicate that sub-degree precision in the absolute pointing can be reached within a few weeks of operation.

Detector configurations: IceCube (see Figure 36.7) consists of 5160 Digital OMs (DOMs) installed on 86 strings at depths of 1450 to 2450 m in the Antarctic ice; except for the DeepCore region, string distances are 125 m and vertical distances between OMs 17 m. 324 further DOMs are installed in IceTop, an array of detector stations on the ice surface above the strings. DeepCore is a high-density

sub-array at large depths (*i.e.*, in the best ice layer) at the centre of IceCube.

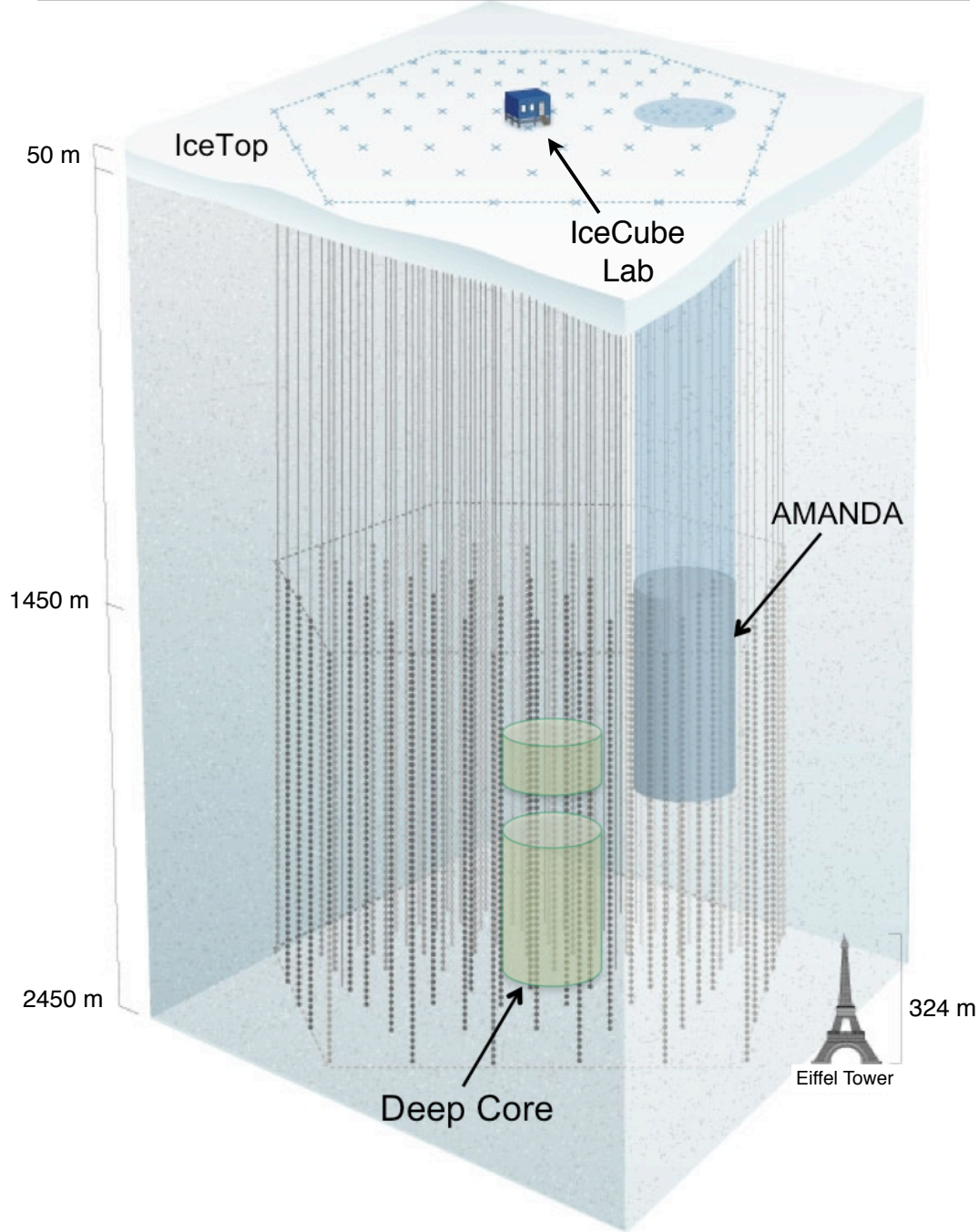


Figure 36.7: Schematic view of the IceCube neutrino observatory comprising the deep-ice detector including its nested dense part DeepCore, and the surface air shower array IceTop. The IceCube Lab houses data acquisition electronics and the computer farm for online processing. Operation of AMANDA was terminated in 2009.

The NT200 detector in Lake Baikal at a depth of 1100 m consisted of 8 strings attached to an umbrella-like frame, with 12 pairs of OMs per string. The diameter of the instrumented volume was 42 m, its height 70 m. Meanwhile (2019), the Baikal collaboration has installed the first five

clusters of a future cubic-kilometre array. A first phase, covering a volume of about  $0.4\text{ km}^3$ , will consist of 9 clusters, each with 288 OMs at 8 strings; its completion is scheduled for 2021. A next stage could comprise about 20 clusters and cover up to  $1.5\text{ km}^3$ .

ANTARES comprises 12 strings with lateral distances of 60–70 m, each carrying 25 triplets of OMs at vertical distances of 14.5 m. The OMs are located at depths of 2.1–2.4 km, starting 100 m above the sea floor. A further string carries devices for calibration and environmental monitoring. A system to investigate the feasibility of acoustic neutrino detection has also been implemented.

KM3NeT will consist of building blocks of 115 strings each, with 18 OMs per string. Operation of prototypes and the first strings deployed have successfully verified the KM3NeT technology [53]. In the upcoming phase 2.0 of its staged implementation, KM3NeT aims at two building blocks for neutrino astronomy, with vertical distances between OMs of 36 m and a lateral distance between adjacent strings of 90 m (ARCA, for *Astroparticle Research with Cosmics in the Abyss*) and at one block for the measurement of the neutrino mass hierarchy, with vertical distances between OMs of 9 m and a lateral distance between adjacent strings of about 20 m (ORCA, for *Oscillation Research with Cosmics in the Abyss*) [50]. A first installation phase of ARCA near Capo Passero, East of Sicily and of ORCA near Toulon has started in 2015 and comprises 24 (6) ARCA (ORCA) strings to be deployed by 2021 (2019). Completion of the full ARCA (ORCA) arrays is planned for 2026 (2024). The possibility of directing a neutrino beam from the Protvino accelerator to ORCA (P2O) is also under study [54].

#### 36.3.2.4 Results

Atmospheric neutrino fluxes have been precisely measured with AMANDA and ANTARES ( $\vec{\nu}_\mu$ ) and with IceCube ( $\vec{\nu}_\mu, \vec{\nu}_e$ ); the results are in agreement with predicted spectra.

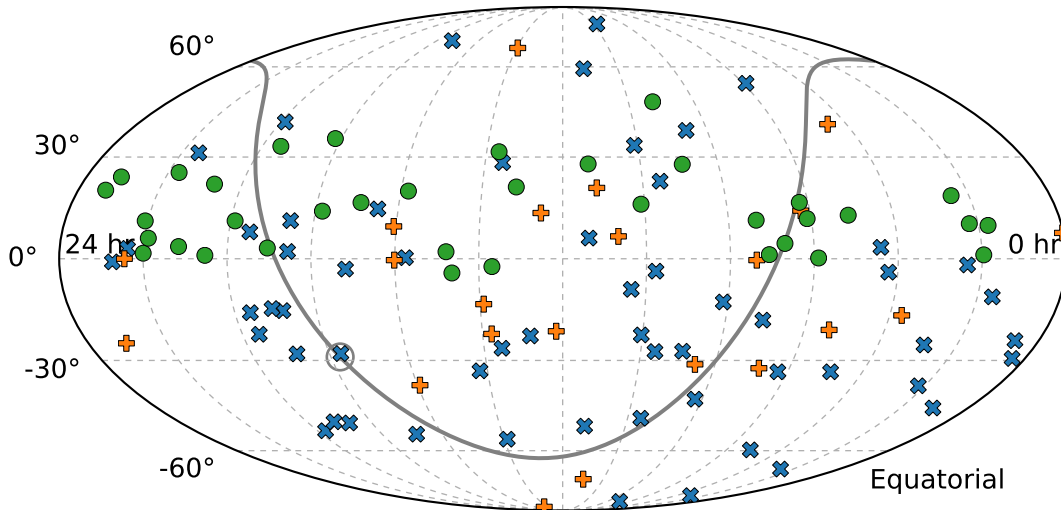


Figure 36.8: Arrival directions of IceCube candidate events for cosmic neutrinos in equatorial coordinates. The plot contains 82 HESE events, with shower-like events marked as blue  $\times$  and muon tracks as orange  $+$ , and in addition 36 through-going muons tracks with an energy deposit exceeding 200 TeV (green circles). Approximately 40% of the events are expected to originate from atmospheric backgrounds. The grey curve denotes the Galactic Plane and the grey circle the Galactic Centre (from [55]).

In 2013, an excess of track and cascade events between 30 TeV and 1 PeV above background expectations was reported by IceCube; this analysis used the data taken in 2010 and 2011 and for the first time employed containment conditions and an atmospheric muon veto for suppression

of down-going atmospheric neutrinos (High-Energy Starting Event analysis, HESE). The observed excess reached a significance of  $5.7\sigma$  in a subsequent analysis of 3 years of data [56] and increased in significance since then. It cannot be explained by atmospheric neutrinos and misidentified atmospheric muons alone. A consistent observation has also been made by ANTARES [57], albeit with much lower significance. The skymap of HESE and high-energy through-going muon events (see Figure 36.8) does not indicate statistically significant event clusters, nor deviations from an isotropic cosmic neutrino flux. Meanwhile the energy range of the IceCube HESE analysis has been extended down to 1 TeV and the high-energy excess confirmed; also, events with through-going muons showed a corresponding excess of cosmic origin. In [58], the various analyses have been combined. Assuming the cosmic neutrino flux to be isotropic, flavour-symmetric and  $\nu$ - $\bar{\nu}$ -symmetric at Earth, the all-flavour spectrum is well described by a power law with normalisation  $6.7_{-1.2}^{+1.1} \times 10^{-18} \text{ GeV}^{-1} \text{ s}^{-1} \text{ sr}^{-1} \text{ cm}^{-2}$  at 100 TeV and a spectral index  $-2.50 \pm 0.09$  for energies between 25 TeV and 2.8 PeV. A spectral index of  $-2$ , an often quoted benchmark value, is disfavoured with a significance of  $3.8\sigma$ .

Multi-messenger observations triggered by a high-energy IceCube neutrino event in 2017 (see Figure 36.9 for an event display), together with a neutrino excess from the same celestial direction in the 2014/15 archival IceCube data, yielded evidence for a first neutrino signal related to a known astronomical object, the blazar<sup>2</sup> TXS 0506+056 [59, 60]. Multi-messenger investigations in conjunction with gravitational waves, ultra-high-energy cosmic rays or gamma-ray observations have not revealed further matching neutrino signals to date. Also, no further astrophysical neutrino sources were found in a recent combined IceCube/ANTARES search for steady sources [61].

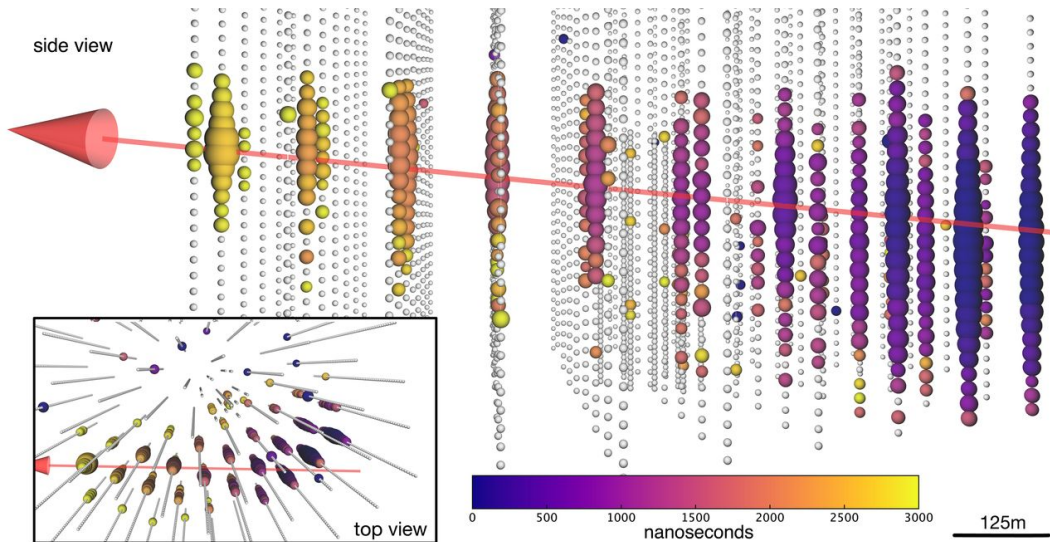


Figure 36.9: Display of the neutrino event IceCube-170922A pointing to the blazar TXS 0506+056. The deposited energy is 24 TeV, the neutrino energy is estimated to be 290 TeV. The colour code indicates the signal timing (blue: early; yellow: late), the size of the coloured circles is a logarithmic measure of the light intensity registered per DOM. The arrow indicates the reconstructed direction, corresponding to a zenith angle of  $5.7_{-0.3}^{+0.5}$  degrees below horizon. Figure from [59].

IceCube has reported an energy-dependent anisotropy of cosmic-ray induced muons and a measurement of the neutrino-nucleon cross section using neutrino absorption in Earth.

No indications for neutrino fluxes from dark matter annihilations or for other exotic phenomena

<sup>2</sup>An Active Galactic Nucleus with a relativistic jet outflow pointing to the observer.

have been found.

At lower energies, down to 10 GeV, IceCube/DeepCore and ANTARES have identified clear signals of oscillations of atmospheric neutrinos. The closely spaced OMs of DeepCore allow for selecting a very pure sample of low-energy  $\bar{\nu}_\mu$  (6–56 GeV) that produce upward moving muons inside the detector. The neutrino energy is determined from the energy of the hadronic shower at the vertex and the muon range. Fits to the energy/zenith-dependent deficit of muon neutrinos provide constraints on the oscillation parameters  $\sin^2 \theta_{23}$  and  $\Delta m_{23}^2$ . The analysis of the same dependence for cascade-like events provides a  $3\sigma$  evidence for  $\nu_\tau$  appearance – an important measurement to test the unitarity of the PNMS matrix [62].

See [63] and [64] for summaries of recent results of IceCube and ANTARES/KM3NeT, respectively.

### 36.3.2.5 Plans beyond 2020

Within the future IceCube-Gen2 project, it is planned to extend the sensitivity of IceCube towards both lower and higher energies. A substantially denser instrumentation of a sub-volume of DeepCore would lead to an energy threshold for neutrino detection of a few GeV, aiming primarily at measuring the neutrino mass hierarchy. For higher energies, a large-volume extension, combined with a powerful surface veto, is envisaged [52]. A very first phase with 7 closely spaced strings is in preparation for deployment in 2022/23, aiming to cover part of the low-energy program, to better calibrate the existing IceCube detector and the archival data, and to test new technologies. More information on the future extensions of GVD and KM3NeT are given above, in Table 36.3 and in [50].

### 36.3.3 Radio emission from (ultra-)high energy particle showers

Revised October 2019 by S.R. Klein (NSD LBNL; UC Berkeley).

Coherent radio-frequency (RF) electromagnetic radiation is an attractive signature to search for particle cascades produced by interactions of high-energy particles. RF signatures have been used to study both cosmic-ray air showers and to search for neutrino-induced showers. The difference in length scale ( $X_0$ ) between air and the solid materials used for other neutrino searches leads to surprisingly large differences in signal generation. This article will begin with neutrino-induced showers, with air showers covered in subsection 36.3.3.3. At lower energies, incoherent optical Cherenkov radiation is frequently used, as discussed in "Neutrino telescopes" section 36.3.2.

RF detectors can be used to search for energetic neutrinos from three types of sources: astrophysical objects (*i.e.* extending measurements the neutrino energy spectrum observed at TeV to PeV energies upward in energy), searching for cosmogenic neutrinos associated with cosmic-ray-cosmic microwave background radiation interactions, and searching for neutrinos from beyond-standard-model physics. These types are roughly associated with energies below  $10^{18}$  eV, the energy range  $10^{18}$  to  $10^{20}$  eV, and above  $10^{20}$  eV. Cosmogenic neutrinos are produced when ultra-high energy (UHE) protons with energy  $E > 4 \times 10^{19}$  eV interact with photons from the cosmic-microwave background radiation, infrared light from old stars, and other extragalactic background light. These protons are excited to a  $\Delta^+$  resonance which may decay via  $\Delta^+ \rightarrow n\pi^+$ , leading to the production of neutrinos with energies above  $10^{18}$  eV [65, 66]. Neutrinos are the only long-range probe of the ultra-high energy cosmos, because protons, heavier nuclei and photons with energies above  $5 \times 10^{19}$  eV are limited to ranges of less than 100 Mpc by interactions with the CMB and early starlight.

The cosmogenic neutrino signal depends heavily on the fraction of UHE cosmic-rays that are protons. For a 100% proton composition (disfavored by most data), observing a cosmogenic neutrino signal of at least a few events per year requires a detector with an active volume of about  $100 \text{ km}^3$ , made out of a non-conducting solid (or potentially liquid) medium, with a long absorption length

for radio waves. The huge volumes require that this be a common material. A dense medium would reduce the detector volume, but, unfortunately, the available natural media have only moderate density. Optical Cherenkov and acoustical detectors are limited by short ( $< 300$  m) attenuation lengths [67] so would require a prohibitively expensive number of sensors. Radio-detection is the only current approach that can scale to this volume. The two most commonly used media are glacial ice, in Antarctica or Greenland, or the lunar regolith [68].

Electromagnetic and hadronic showers produce radio pulses via the Askaryan effect [69, 70], as discussed in "Passage of Particles Through Matter" review Sec. 34. The shower contains more electrons than positrons. At wavelengths longer than the transverse size of the shower, this leads to coherent Cherenkov emission, where the electric field scales as the square of the net charge excess. This may also be described more generally as being due to radiation from a time-varying net charge [71]; this latter description also applies to radio emission in cosmic-ray air showers.

High-frequency radiation is concentrated around the Cherenkov angle. Viewed directly on the Cherenkov cone, the electric field strength,  $\epsilon_{\text{Ch}}$  at a frequency  $f$  from an electromagnetic shower from a  $\nu_e$  may be roughly parameterized as [72, 73]

$$\epsilon_{\text{Ch}}(\text{V/mMHz}) = 2.53 \times 10^{-7} \frac{E_\nu}{1\text{TeV}} \frac{f}{f_c} \left[ \frac{1}{1 + (f/f_c)^{1.44}} \right]. \quad (36.3)$$

The electric field strength increases linearly with frequency, up to a cut-off frequency  $f_c$ , which is set by the transverse size of the shower [74, 75]. The maximum wavelength  $c/f_c$  is roughly the Moliere radius divided by  $\cos(\theta_C)$  where  $\theta_C$  is the Cherenkov angle. The cutoff frequencies depend on the density (which affects the Moliere radius). They are about 1 GHz in ice, and about 3 GHz in the lunar regolith. Near  $f_c$ , radiation is narrowly concentrated around the Cherenkov angle [74, 75]. At lower frequencies, the limited length of the emitting region leads to a broadening in emission angle around the Cherenkov cone. Away from  $\theta_C$ , the electric field from Eq. (36.3) is reduced by [72],

$$\frac{\epsilon}{\epsilon_{\text{Ch}}} = \exp \left( -\frac{1}{2} \frac{(\theta - \theta_C)^2}{(2.2^\circ \times [1\text{GHz}/f])^2} \right). \quad (36.4)$$

In both ice and the lunar regolith, the Cherenkov angle is about  $56^\circ$ . At very low frequencies, the distribution is very broad, with  $f = 50\text{MHz}$  corresponding to a shower with an angular spread of  $\sigma = 45^\circ$ .

More accurate calculations of the predicted radio signal from a neutrino require detailed Monte Carlo simulations. These simulations begin with a neutrino induced shower, and then calculate (directly or from a parameterization) the Askaryan signal. The Askaryan signal calculation is tough for two reasons. First, much of the excess charge comes from the lowest energy particles in the shower. Second, it is necessary to keep track of the phase of the signal from each particle, as well as the amplitude and the time (or frequency) dependence. This signal is then propagated through the medium and into an antenna model [73].

Along the Cherenkov cone, the 1 GHz maximum frequency leads to a generated pulse width of  $\approx 1$  nsec. This pulse broadens by dispersion as it propagates, particularly for signals from the Moon traversing the ionosphere. As long as the dispersion can be compensated for and backgrounds controlled, a large bandwidth detector is the most sensitive. Spectral information can be used to reject background, and to help reconstruct the neutrino direction, because the cutoff frequency depends on the observation angle with respect to the Cherenkov cone.

The electric field is linearly proportional to the neutrino energy, so the power (field strength squared) is proportional to the square of the neutrino energy. Since the signal is a radio wave, the field amplitude decreases as  $1/R$ , plus absorption in the intervening medium. The detection

threshold is determined by the distance to the antenna and the noise characteristics of the detector. For an antenna located in the detection medium, the typical threshold is around  $10^{17}$  eV; for stand-off (remote sensing) detectors, the threshold rises roughly linearly with the distance. These thresholds can be reduced significantly by using directional antennas and/or combining the signals from multiple antennas using beam-forming techniques. Experiments have used both approaches to reduce trigger-level noise, or to reject background at the analysis level. For multi-element arrays, the threshold drops as the square root of number of antennas, since the signal adds in-phase while the backgrounds add with random phases [76].

Some common background sources are anthropogenic noise, antenna/preamp noise, cosmic-ray air showers, charge generated by blowing snow, lightning, and, at low frequencies, radiation from the Milky Way. The need to limit anthropogenic noise has led most experimental groups to select remote locations for their detectors.

Reconstruction of the neutrino arrival direction depends on several aspects of the signal. First, the direction from the antenna to the interaction site must be determined. This can be done by using the relative timing from separated antennas, or using beam-forming techniques with multi-element arrays. If the radio signal encounters media where the index of refraction vary (like the firm of glacial ice), then it may be necessary to use ray-tracing techniques to follow the signal back to interaction point. The distance (and hence the neutrino energy) can be difficult to determine unless the signal can be triangulated, either using multiple, separated antennas, or observing two pulses with different flight paths (*i. e.* with one including a reflection) in a single antenna.

The neutrino arrival direction can be determined with respect to that direction via two angles, which are determined using very different methods. The first uses the measured frequency spectrum. Equation 36.4 can be used to determine the angular distance between the detector vector and the Cherenkov cone. The second angle can be determined by the polarization of the signal. The radio signal is produced with a linear polarization in the plane containing both the neutrino direction and the photon direction. These two angles can be combined to determine the direction, subject to a (usually) four-fold ambiguity, due to uncertainty as to whether the antenna is inside or outside the Cherenkov cone, and because the neutrino direction can be flipped  $180^\circ$  without affecting the observed signal. Often, some of these solutions can be rejected because they correspond to long path lengths through the Moon or the Earth, where the neutrino would be absorbed.

At energies above  $10^{16}$  eV in ice, the Landau-Pomeranchuk-Migdal effect lengthens electromagnetic showers, by reducing the cross-sections for bremsstrahlung and pair production [77]. The lengthening of the shower leads to a narrowing of the radio emission around the Cherenkov cone, and a reduction in high-frequency emission away from the cone [73]. At higher energies, this leads two separate components of the Askaryan radiation: an un-altered component from the hadronic portion of the shower (on average 20% of the total energy) and an angularly narrowed component from the LPM-lengthened electromagnetic shower. The angular narrowing scales as  $E_\nu^{1/3}$ ; If these two components can be observed separately, they could, in principle, be combined to determine the inelasticity of the neutrino interaction [78], allowing for improved measurements of parton distributions, and searches for beyond-standard-model interactions.

At still higher energies, above  $10^{20}$  eV, the LPM effect becomes stronger, and the electromagnetic shower splits into multiple subshowers with significant separation. When this separations become large enough, the subshowers will effectively become independent radiators, with the total emission showing substantial event-by-event variation, depending on the division into subshowers [77]. Because of this, many of the experiments that study higher energy (well above  $10^{20}$  eV) neutrinos focus on the hadronic shower from the struck nucleus. This contains an average of only about 20% of the energy, but with smaller large fluctuations.

Figure 36.10 shows some of the current limits from neutrino searches, including from prototype arrays. Except for LOFAR, which is fully operational, projected limits from future experiments are not shown in the figure.

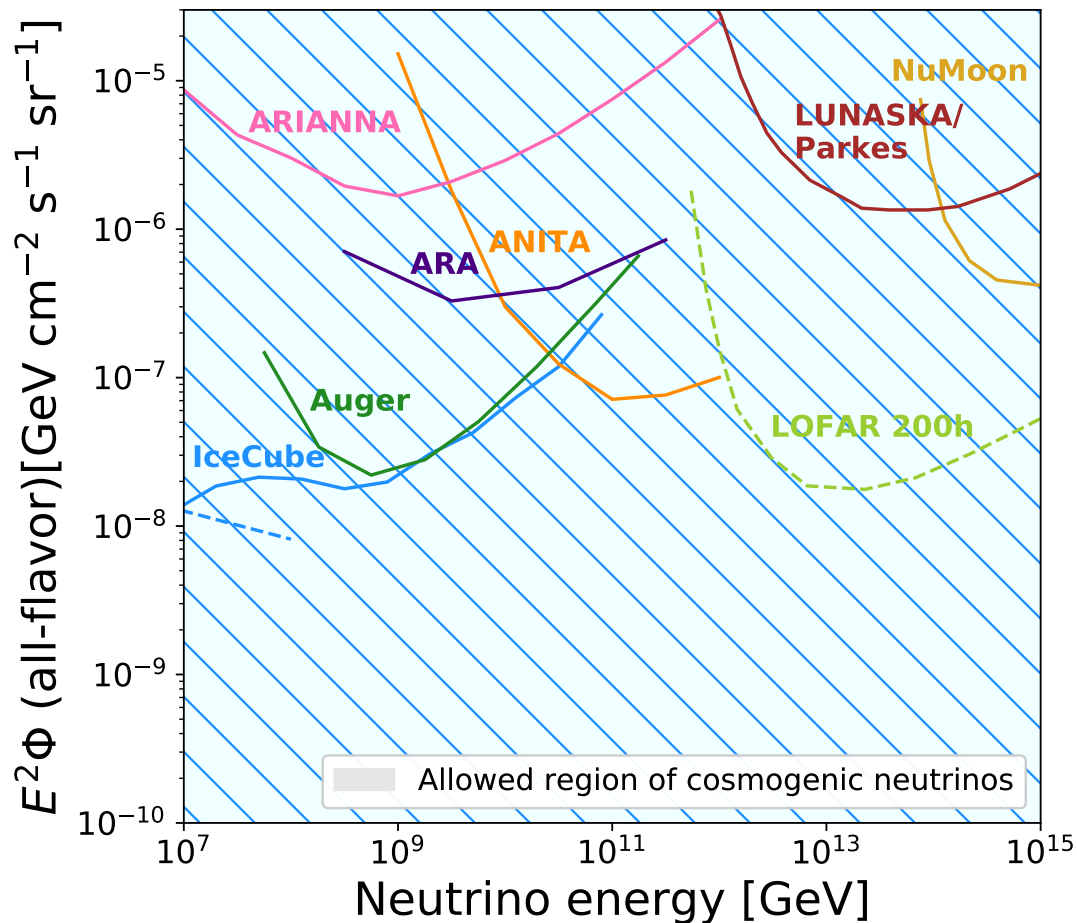


Figure 36.10: Representative 3-flavor (summed, assuming equal fluxes of each flavor) differential (over one decade in energy) limits from different experiments and prototype experiments. Shown are limits from the IceCube ultra-high energy  $\nu$  search [79], the Auger search for earth-skimming  $\nu_\tau$  [80], the LUNASKA/Parkes [81] and NuMoon lunar searches [82], the ANITA balloon experiment [83], ARA [84] and ARIANNA prototypes [85], along with projections for the LOFAR array [86]. The dashed blue line is the extrapolation of the IceCube through-going  $\nu_\mu$  flux measured at lower energies (few 10s of TeV to 10 PeV), with spectral index  $\alpha = -2.28$  [87]. Because of the long extrapolation, this should only be treated as a rough reference. The ARA and ARIANNA limits are from prototype arrays, and indicate the energy range that might be covered, with far higher sensitivity by larger arrays. The shaded area is the allowed region for neutrinos, from a recent global analysis that included the measured cosmic-ray spectrum and composition [88]. Thanks to Anna Nelles (DESY-Zeuthen) for preparing this figure, which is adapted from Ref. [89].

One variation on the radio-detection approach is to look for radio signals from Earth-skimming  $\nu_\tau$ . Although  $\nu_\tau$  are much less commonly produced than  $\nu_\mu$  and  $\nu_e$ , as they travel astrophysical distances, oscillations lead to a  $\nu_e : \nu_\mu : \nu_\tau$  ratio near 1 : 1 : 1, for almost all non-exotic acceleration and propagation mechanisms [90].

If the  $\nu_\tau$  traverse the Earth and interact while traveling upward, near the surface, the resulting

$\tau^\pm$  may exit the Earth before decaying. 83% of the time, the decay produces a hadronic or electromagnetic shower in the atmosphere [91]. Experiments have searched for this upgoing shower, and for the resulting optical Cherenkov and coherent RF radiation. The threshold energy dependence for these searches depends on several factors, notably including the average  $\tau^\pm$  decay length, which increases linearly with energy; the Pierre Auger observatory set limits on the neutrino flux at energies above  $10^{17}$  eV [80]. Radio-detection efforts have similar or slightly higher thresholds. Detection in low-density (compared to rock or ice) air introduces a number of new complications, including the much larger length scale and the effects of the Earth's magnetic field. These issues are similar to those inherent in studies of radio signals from cosmic-ray air showers, discussed later.

The ANITA balloon-based radio-detection experiment has even reported two anomalous events [92] which the collaboration has indicated might be from Earth-skimming  $\nu_\tau$ . However, this interpretation is controversial.

A number of prototype  $\nu_\tau$  radio-detection experiments exist. The GRAND Collaboration recently proposed to deploy a 10,000 antenna array, eventually growing to 200,000 antennas spread over 200,000 km<sup>2</sup> [93]. The latter array would be sensitive to cosmogenic neutrinos, unless the UHE cosmic-ray flux is mostly heavier nuclei.

Magnetic monopoles would also emit radio waves, and neutrino experiments have also set monopole flux limits [94].

### 36.3.3.1 The Moon as a target

Because of its large size and non-conducting regolith, and the availability of large radio-telescopes, the Moon is an attractive target [95]. Conventional radio-telescopes are quite well suited to lunar neutrino searches, with natural beam widths not too dissimilar from the size of the Moon. Still, there are experimental challenges. The attenuation length is typically estimated to be  $9m/f(\text{GHz})$ , so only near-surface interactions can be studied. The composition of the lunar regolith is not well known, so there are significant uncertainties on this attenuation. And, there is a background from cosmic-ray interactions in the Moon. One big limitation of lunar experiments is that the 240,000 km target-antenna separation leads to neutrino energy thresholds above  $10^{20}$  eV.

The effective volume probed by experiments depends on the geometry, which itself depends on the frequency range used. At high frequencies  $f$ , the electric field strength is high, leading to a lower energy threshold, but the sensitive volume is limited because the Cherenkov cone only points toward the Earth for a narrow range of geometries. Lower frequency radiation is more isotropic, so the effective volume is larger, but, because the electric field is weaker, the energy threshold is higher. The  $1/f$  dependence of the attenuation length in the lunar regolith further increases the effective volume at low frequencies. The frequency range affects the energy dependence of the sensitivity. As can be seen in Fig. 36.10, a low-frequency experiment like NuMoon (which covered 115-180 MHz) has good sensitivity, but only above about  $10^{14}$  GeV, while Lunaska/Parkes, which observed in the range 1200-1500 MHz, has a higher flux limit, but is sensitive above about  $10^{12.5}$  GeV.

With modern technology, it is increasingly viable to search over very broad frequency ranges [96]. One technical challenge is due to dispersion (frequency dependent time delays) in the ionosphere. Dispersion can be largely removed with a de-dispersion filter, using either analog circuitry or post-collection digital processing.

Lunar experiments use different techniques to reduce the anthropogenic background. Some experiments use multiple antennas, separated by at least hundreds of meters; by requiring a coincidence within a small time window, anthropogenic noise can be rejected. With good enough timing, beam-forming techniques can be used to further reduce the background. An alternative approach is to use beam forming with multiple feed antennas viewing a single reflector, to ensure that the

signal points back to the moon.

In the near future, several large radio detector arrays should reach significantly lower limits. The LOFAR array is taking data with 36 detector clusters spread over Northwest Europe [86]. In the longer term, the Square Kilometer Array (SKA) with its  $1 \text{ km}^2$  effective area will push thresholds down to near  $10^{20}$  eV [96]. It should be noted that current limits and projected sensitivities are sensitive to many details, and different analyses make different assumptions. A recent review [97] compared different radio-detection experiments using a common framework, and found some significant shifts in sensitivities.

### 36.3.3.2 *Ice-based detectors*

Detecting neutrinos with a lower energy threshold requires a smaller antenna-target separation. Natural ice is an attractive medium for this, offering a stable construction platform, with radio attenuation lengths from over 300 m to 1 km. The attenuation length varies with the frequency and ice temperature, with higher attenuation in warmer ice.

Although glacial ice is mostly uniform, the top  $\approx 100$  m of ice, the 'firn,' exhibits a gradual transition from packed snow at the surface (typical density  $0.35 \text{ g/cm}^3$ ) to solid ice (density  $0.92 \text{ g/cm}^3$ ) below [98]. The thickness of the firn varies with location; it is thicker in central Antarctica than in the coastal ice sheets or in Greenland. The varying density has several implications.

The index of refraction depends linearly on the density, so radio waves curve downward in the firn. This bending reduces the effective volume of surface or aerial antennas. A surface antenna cannot see near-surface interactions at large horizontal distances. The bending also means that the arrival direction of radio waves do not point directly back to the neutrino source. One must use ray tracing to determine the direction of neutrino interactions.

The bending also creates an opportunity to measure the distance from the detector to the neutrino interaction. For some geometries with buried antennas, there may be two paths to the detector: one 'direct' path, with minor bending, and a second where the signal is bent beyond vertical, bouncing off the surface before reaching the antenna. By measuring the time difference between the two paths, the distance to the interaction vertex may be determined; this greatly improves the energy determination [99, 100].

There are also indications that the increase in firn density is non-monotonic [101, 102]. This can lead to a non-monotonic change in index of refraction which may create waveguides which trap a small fraction of the radio energy and propagate it horizontally.

In one type of experiment, antennas mounted on scientific balloons observe the ice from above. Radio signals from in-ice neutrino interactions propagate to the surface, traverse the ice-air interface, and then travel to the balloon. The surface roughness of the ice can affect signals as they transition from the ice to the atmosphere. The best known example, ANITA, has made four flights around Antarctica, floating at an altitude around 35 km [103]. Its 32/40/48 (depending on the flight) dual-polarization horn antennas scanned the surrounding ice, out to the horizon (650 km away). Because of the small angle of incidence, ANITA could use polarization to separate signals from background;  $\nu$  signals should be vertically polarized, while most background from cosmic-ray air showers should be horizontally polarized.

Because of the significant source-detector separation, ANITA is most sensitive at energies above  $10^{19}$  eV, above the peak of the cosmogenic neutrino spectrum. As with all radio-detection experiments, ANITA had to contend with anthropogenic backgrounds. The ANITA collaboration uses their multiple antennas as a phased array to achieve good pointing accuracy. They rejected all events that pointed toward known or suspected areas of human habitation. By using the several-meter separation between antennas, they achieved a pointing accuracy of  $0.2\text{-}0.4^\circ$  in elevation, and  $0.5\text{-}1.1^\circ$  in azimuth. ANITA has set the most stringent flux limits yet on neutrinos with energies

above  $10^{20}$  eV [83].

Other ice based experiments use antennas located within the active volume, allowing them to reach thresholds around  $10^{17}$  eV, or lower with phased array antennas. This approach was pioneered by the RICE experiment [104] which buried 18 half-wave dipole antennas in holes drilled for AMANDA at the South Pole, at depths from 100 to 300 m. The hardware was sensitive from 200 MHz to 1 GHz. Each antenna fed an in-situ preamplifier which transmitted the signals to surface digitizing electronics.

Two groups have deployed prototype arrays which have explored different detector concepts. The Askaryan Radio Array (ARA) deployed surface and buried antennas at the South Pole [105], while the Antarctic Ross Iceshelf Antenna Neutrino Array (ARIANNA) installed surface antennas on the Ross Ice Shelf [85], about 110 km north of McMurdo station. ARIANNA offered the possibility of detecting downward-going  $\nu$ , from the radio waves reflected off the ice-sea water interface on the bottom of the Ross Ice Shelf, while ARA took advantage of the colder ice at the South Pole, with its longer radio attenuation length. ARA buried antennas up to 200 m deep, be able to observe a larger portion of ice, due to the refraction of the signal in the firn. In contrast, ARIANNA deployed antennas just below the surface, allowing them to use high-gain, but large log periodic dipole antennas. Recently, phased-array trigger techniques have been demonstrated that can reduce the energy threshold by a factor of several [76, 106].

Both experiments use stations which operate independently, spaced far enough to maximize sensitivity, but where only a small fraction of neutrino events will be visible in multiple stations. Each station includes multiple antennas, which will include both horizontal and vertical polarization. The collaborations can determine the neutrino arrival direction (modulo a (usually) 4-fold directional ambiguity) by using relative timing to find the direction from the station to the interaction, and the neutrino arrival direction by using the frequency spectrum to find the angular distance from the Cherenkov cone and by measuring the linear polarization of the radio signal. The expected angular resolution is a few degrees.

Looking ahead, the RNO [89] and ARIANNA [107] Collaborations have proposed next-generation experiments combining the best features from ARA and ARIANNA. Both experiments have been proposed for the South Pole, although operation in Greenland may also be considered. Further out, the proposed IceCube Gen2 expansion includes a substantial radio array component [52]

### 36.3.3.3 *Radio-detection of cosmic-ray air showers*

The physics of radio-wave generation in air showers is more complex than for neutrino-induced showers [108], although there are enough similarities that some experiments are sensitive to both sources. Particularly in the upper atmosphere, air is much less dense than rock or ice, so the showers develop over much larger distance scales. These larger distance scales lead to significant effects from the Earth's magnetic field.

For cosmic-rays arrival directions that are perpendicular to the magnetic field, the field produces significant charge separation, as electrons and positrons are bent in different directions as they propagate. This leads to a growing charge dipole (transverse current) [109]. This time-varying transverse current emits radiation, spread over the transverse size of the shower, with a Cherenkov ring around the primary trajectory. Electrons in the shower may also emit synchrotron radiation due to bending in the Earth's field. Since the radiating particles are moving relativistically downward, a ground-based observer sees a Lorentz contracted pulse which can have frequency components reaching the GHz range, limited by the thickness of the particle shower. However, for most geometries, the bulk of the energy is at frequencies below 100 MHz, and most experiments are focused at frequencies below that.

There is still a contribution from coherent radio Cherenkov signals, but it is subdominant.

Its most notable effect is to create an azimuthal (around the shower axis) interference pattern, destroying the radial symmetry of the radiation [110].

Since they observe the atmosphere, one of the major issues for radio-detection experiments is anthropogenic noise. Most man-made noise has distinctive characteristics (such as being narrow-band, and coming from near the horizon) which makes it relatively easy to reject during data analysis, via narrow-band filters and other techniques [111]. However, these factors complicate triggering. This is even an issue in Antarctica, where communication radios and passing satellites can mimic showers, at least at the trigger level. For this reason, most experiments have used radio antennas in combination with at least one other detector technology, such as scintillation counters. One exception is ARIANNA, which is located in an uninhabited part of Antarctica, enabling them to self-trigger on air showers [112]. With careful choice of frequency band, it may be possible to reach PeV energies with Antarctic detectors [113]. In more populous areas, the triggering challenges are likely to be bigger.

Radio-detection can be used to determine the shower energy, as done by the Auger and Tunka-Rex experiments [114,115]. Radio signals can also be used to infer the altitude for shower-maximum, where the shower contains the most particles, as done by the LOPES and Tunka-Rex collaborations [115,116]. This altitude is sensitive to the cosmic-ray composition. Radio-detection is also useful for energy cross-calibrations between different experiments, and, with improved simulations, may be able to provide an independent energy scale calibration for air shower arrays.

### 36.4 Large time-projection chambers for rare event detection

Revised October 2019 by T. Shutt (SLAC).

Rare event searches require detectors that combine large target masses and low levels of radioactivity, and that are located deep underground to eliminate cosmic-ray related backgrounds. Past and present efforts include searches for the scattering of particle dark matter, neutrinoless double beta decay, and the measurement of solar neutrinos, while next generation experiments will also probe coherent scattering of solar, atmospheric and diffuse supernova background neutrinos. Large time project chambers (TPCs) [117], adapted from particle collider experiments, have emerged as a leading technology for these efforts. Events are measured in a central region confined by a field cage and usually filled with a liquid noble element target. Ionization electrons are drifted (in the  $z$  direction) to an anode region by use of electrode grids and field shaping rings, where their magnitude and  $x - y$  location is measured. In rare event searches (with no external trigger available) scintillation generated at the initial event site is also measured, and the time difference between this prompt signal and the later-arriving charge signal gives the event location in  $z$  for a known electron drift speed. Thus, 3D imaging is achieved in a monolithic central volume. The relatively slow readout due to the drift of charges ( $\sim 1/2$  ms/m at 1 kV/cm) [118] is not a major pile-up concern in low background experiments. Noble elements have relatively high light yields (comparable to or exceeding the best inorganic scintillators), and the charge signal can be amplified by multiplication or electroluminescence. Radioactive backgrounds are distinguished by event imaging, the separate measurements of charge and light, and scintillation pulse shape. For recent reviews of noble element detectors, see [119] [120] [121] [122].

Methods for achieving very low radioactive backgrounds are discussed in general in section 35.6. The basic architecture of large TPCs is very favorable for this application because gas or liquid targets can be relatively easily purified, while the generally more radioactive readout and support materials are confined to the periphery. The 3D imaging of the TPC then allows self shielding in the target material, which is quite powerful when the target is large compared to mean scattering lengths of order  $\sim 10$  cm for  $\sim$  MeV neutrons and gammas from radioactivity. Most recent experiments have immersed the TPCs in hermetic water shields to eliminate external

radioactive backgrounds, and several are also using an active scintillator inner layer to further veto backgrounds from detector materials. While other target fluids are possible, almost all recent efforts have used Xe and Ar. In LHe and LNe the mobility of electrons is  $\sim 10^3$  times lower than in the heavier noble elements due to the formation "bubbles" around electrons. [123] [124] It is worth noting that scintillation and electron drift are possible in a number of organic fluids, possibly providing a route to economical large detectors, but with much reduced performance compared to noble elements.

In noble element targets, all non-noble impurities are readily removed (e.g., by chemical reaction in a commercial getter) so that only radioactive noble isotopes are a significant background concern. Xe, Ne and He have no long lived radioactive isotopes (apart from the  $^{136}\text{Xe}$ , discussed below, and the very long-lived  $^{124}\text{Xe}$  [125]). Kr has  $\sim 0.3$  MBq/kg of the beta emitter  $^{85}\text{Kr}$  created by nuclear fuel reprocessing [126], making it unusable as a target, while the  $\sim 1$  Bq/kg level of the beta emitter  $^{39}\text{Ar}$  [127] is a nuisance for Ar-based experiments. Both of these can be backgrounds in other target materials, as can Rn emanating from detector components. Relatively low background materials are available for most of the structures surrounding the central target, with the exception of radioactive glasses and ceramics usually present in PMTs, feedthroughs and electrical components. Very low background PMTs with synthetic quartz windows, available over the last 15 years (see, e.g., [128]), have been a key enabling technology for dark matter searches. Radio-clean SiPMs and related Si-based photon detectors are increasingly being used in cases where their dark rates (which are significantly higher than PMTs) can be tolerated.

An important technical challenge in liquid detectors is achieving the high voltages needed for electron drift and measurement. In general, quench gases which stabilize charge gain and speed electron transport in wire chambers cannot be used, since these absorb and/or quench scintillation light and can trap electrons. It is also important to suppress low-level emission of electrons and associated photons which can otherwise swamp low energy signals. Drift of electrons over meter scales with minimal loss from attachment on trace levels of dissolved impurities (e.g.,  $\text{O}_2$ ) has so far required continuous circulating purification.

#### 36.4.1 Dark matter and other low energy signals

A major goal of low background experiments is detection of WIMP (Weakly Interacting Massive Particle) dark matter through scattering on nuclei in a terrestrial detector (for a recent review, see [129]). Energy transfers are generally small, a few tens of keV at most. Liquid noble TPCs distinguish single nuclear recoils (NR) from dark matter from the dominant background of electron recoils (ER) from gamma rays and beta decays by rejecting multiple scatters, and, as described below, based on both the ratio of charge to light and the scintillation pulse shape. Neutrons are a NR background, but are present at much lower rates than gammas and betas, and also undergo significant multiply scattering. To detect small charge signals, a dual phase technique is used wherein electrons from interactions in the liquid target are drifted to the liquid surface and extracted with high field ( $\sim 5$  kV/cm) into the gas phase where they create an amplified electroluminescence signal which is usually measured by an array of PMTs located just above the liquid. (While both charge multiplication and electroluminescence are possible in liquid, they require very high fields created by very small electron structures and thus have not seen widespread adoption. For recent progress see [130]) This technique readily measures single electrons with  $\sim \text{cm } x - y$  resolution.

The measurement of the initial scintillation signal, by contrast, suffers from loss upon reflection from the TPC walls, and inefficiency in the readout, and usually limits the energy threshold. In LXe, the  $\sim 178$  nm wavelength is just long enough to be transmitted through high purity synthetic quartz PMTs windows, and, remarkably, PTFE immersed in LXe has  $\sim 97\%$  reflectivity. [131] The  $\sim 128$  nm scintillation light of LAr requires waveshifting (usually using TPB) both for reflectivity

(usually on PTFE) and for efficient measurement. With both liquids, a second sensor array at the bottom of the TPC is used to maximize light collection, and total photon efficiencies have been in the 10-15% range. Typical raw yields for ER are several tens of electrons and photons per keV, and, in LXe, a NR threshold of  $\sim 5$  keV has been achieved [132].

The microscopic processes leading to signals in liquid nobles are complex. Energy deposited by an event generates pairs of free electron and ions, and also atoms in their lowest excited state. The latter rapidly form excimers which de-excite by emitting light. Excimers arise in both triplet and singlet states which have the same energy but different decay times. In an event track, some fraction of electrons recombine with ions, while the rest escape and are measured. Each recombined ion creates an additional excimer, and hence another photon. Finally, some part of the energy is lost as heat - a small fraction for ER but a dominant and energy dependent fraction for NR. The branching into these various modes depends on drift field, energy, and particle type, requiring extensive calibrations. These have largely been carried out for LXe (see, e.g., [133]), and have been incorporated into the NEST Monte Carlo framework. [134]

This complexity also gives rise to discrimination between ER and NR: for the same visible energy, the slower NR create short, denser tracks and generate a higher fraction of initial excitons, leading to a smaller ratio of measured charge to light. NR also generate a higher ratio of short-lived singlet state to long-lived triplet states than ER, so that the scintillation signal itself gives pulse shape discrimination (PSD). Charge/light discrimination has been well mapped in LXe, and, remarkably, is very high (>99.9%) below  $\sim 10$  keV for NR. [132] It has only recently been measured in LAr [135], and has not yet played an important role in LAr based experiments. Qualitatively, PSD is similar in LXe and LAr - strong at high energy and weak at low energy. However it is well mapped only in LAr where it is very high above  $\sim 50$  keV, achieving values above  $\sim 10^8$ . [136]

This extremely powerful PSD in LAr is sufficient to overcome the ER background from  $^{39}\text{Ar}$ , which is roughly  $10^7$  times higher than the fundamental low energy ER background from p-p solar neutrinos. In a multi-ton detector the event rate from  $^{39}\text{Ar}$  poses a significant pile-up challenge, and the DarkSide collaboration is pursuing  $^{39}\text{Ar}$  reduction through two methods. One, for which a factor 1400 reduction in  $\sim 50$  kg Ar has been demonstrated, is extracting “aged” Ar from underground (cosmic ray shielded) gas deposits in which the 269 yr half-life  $^{39}\text{Ar}$  has decayed. [137] The other method is removal by distillation. The need for  $^{39}\text{Ar}$  depleted Ar negates the much lower raw material cost of Ar compared to Xe. Kr must also be removed from both Xe and Ar experiments (and Ar must be from Xe experiments), comparatively easy tasks compared to isotopic separation. This is done through distillation or a chromatographic technique. In current LXe experiments the remaining dominant ER backgrounds is the beta decay of a daughter of  $^{222}\text{Rn}$  in the active LXe, where the Rn has emanated from detector materials or external plumbing. Rn will be even more important as experiments scale up in size, but can in principle be reduced by better materials screening and online Rn separation, again by either distillation or chromatography. Neutrons are in general some six orders of magnitude less abundant than gamma rays and betas in U and Th decay chains, but they naturally scatter in the WIMP energy range, and their single scatters cannot be discriminated against. Self shielding is less powerful for neutrons than gamma rays, so that they are an increasingly important background at the current ton scale and future larger experiments, both in Ar and Xe. Active outer shielding layers which tag and veto neutrons are being included in most next generation experiments.

The WIMP sensitivity is a combination of backgrounds, discrimination, and WIMP scattering rates. The scattering rates are model dependent, but are in general dominated by spin-independent coherent scattering on the full nucleus. This has an  $A^2$  dependence, favoring high mass targets. The energy spectrum is close to a falling exponential, so that the lowest possible energy threshold maximizes sensitivity. Experiments using LXe TPCs have had the leading sensitivity for standard

WIMP dark matter for well over a decade, for all but the lowest WIMP masses. The ton-scale XENON1T [138] achieved a WIMP-nucleon sensitivity of  $4.1 \times 10^{-47} \text{ cm}^2$  at 30 GeV mass, closely followed by PANDAX-II [139] and LUX [140]. The next generation  $\sim 7$  tonne experiments LZ [141] and XENONnT [142], and  $\sim 4$  tonne PandaX-4T [143] are currently in late stages of construction. The DarkSide program is carrying out WIMP searches with LAr TPCs. The 50 kg DarkSide-50 achieved a sensitivity  $\gtrsim 40$  times poorer than XENON1T. A 50 ton scale-up, DarkSide-20 is being pursued which features SiPMs instead of PMTs. [144]. (The best current limit using LAr is not from a TPC, but instead the scintillation-only DEAP-3600 experiment. [136])

LZ and XENONnT project sensitivity to WIMPs about a decade above the “floor” of coherent scattering of astrophysical neutrinos, which, absent a directional measurement (see below), are essentially indistinguishable from WIMPs. DARWIN, a proposed a 50 ton LXe TPC would approach the practical limit set by this floor for WIMP masses above  $\sim 5$  GeV [145], while ARGO a  $\sim 200$  ton LAr detector would achieve similar sensitivity for WIMPs masses well above  $\sim 50$  GeV. [144]

There has been recent interest in models featuring low mass dark matter. These give rise to low energy recoils, and also strongly favor low mass target nuclei (despite the  $A^2$  rate penalty). This has led to renewed focus on events below the scintillation threshold, where the charge signal alone achieves very low threshold due to the gain of the electroluminescence readout. This preserves  $x - y$  spatial information, but only very weak depth information based on electron diffusion. Thus it is subject to the high backgrounds at the top and bottom of the active region, and decays of Rn daughters on grids. While the first such results came from XENON10, a recent result in LAr from DarkSide-50 extends to much lower dark matter mass because of the lower mass of Ar. To maximize the sensitivity of such searches in the future, studies have begun to understand and minimize the sources of electron backgrounds from both radioactivity and spurious sources such as field emission from grids. There is also an effort to develop a superfluid He TPC [146] read out with superconducting sensors (similar to the proposed HERON solar neutrino experiment). The rich set of signals in this case - scintillation, rotons, and ionization - potentially offer significant background rejection.

Measurement of NR recoil track direction would provide proof of the galactic origin of a dark matter signal since the prevailing WIMP direction varies on a daily basis as the earth spins. This cannot be achieved for the sub-micron tracks in any existing solid or liquid technology, but the mm-scale tracks in a low pressure gas (typically,  $P \sim 50$  Torr) could be imaged with sufficiently dense instrumentation. Directionality can be established with  $O(10^2)$  events by measuring just the track direction, while, with finer resolution that distinguishes the diffuse (dense) tail and dense (diffuse) head of NR (ER) tracks, only  $O(10)$  events are required. Such imaging requires a high energy threshold, decreasing WIMP sensitivity, but also powerfully rejecting less dense ER background tracks.

A variety of TPC configurations are being pursued to accomplish this, most with a  $\text{CF}_4$  target. The longest established effort, DRIFT, avoids diffusion washing out tracks for electron drift distances greater than  $\sim 20$  cm by attaching electrons to  $\text{CS}_2$ , which drifts with vastly reduced diffusion. Other efforts drift electrons directly and use a variety of techniques for their measurement: DMTPC (electroluminescence + CCDs), MIMAC (MicroMegs), NEWAGE (GEMs), and  $\text{D}^3$  (Si pixels). A related suggestion is that the amount of recombination in a high pressure Xe gas with an electron-cooling additive could be sensitive to the angle between the track and electric field [147], eliminating the need for track imaging. Directional measurements appear to be the only possibility to push beyond the floor of coherent neutrino scatters [148], though at the cost of enormous target mass and channel count.

### 36.4.2 $0\nu\beta\beta$ Decay

Another major class of rare event search is neutrinoless double beta decay ( $0\nu\beta\beta$ ). A limited set of nuclei are unstable against simultaneous beta decay of two neutrons. Fortunately, this includes the Xe isotope  $^{136}\text{Xe}$  (Q-value 2458 keV), which can be used as the active material in a detector, and which, as an inert gas, can also be more readily enriched from its natural 8.9% abundance than any other  $\beta\beta$  isotope. Observation of the lepton-number violating neutrinoless version of this decay would establish that neutrinos are Majorana particles and provide a direct measure of neutrino mass. For a recent review, see [149] [122]. The signal in  $0\nu\beta\beta$  decay is distinctive: the full Q-value energy of the nuclear decay appears as equal energy back-to-back recoil electrons. A large TPC is advantageous for observing this low rate decay for all the reasons described above. The first detector to observe the standard model process two neutrino double beta decay was a gaseous TPC which imaged the two electrons tracks from  $^{82}\text{Se}$  embedded in a foil. [150] Modern TPCs use Xe as the detector medium.

The dominant background is gamma rays originating outside the active volume. Most of these undergo multiple Compton-scatters which are efficiently recognized and rejected through sub-cm position resolution, though the few percent of gammas at this energy that photoabsorb are not. Self shielding of gamma rays in the double beta decay energy window is less powerful than in the low energy dark matter window, since in the former case there is some small probability of penetrating to some depth followed by the modestly small probability of photo-absorption. The latter case consists of three small probability processes: penetration to some depth, a very low-energy scatter, and the gamma exiting without a second interaction. Because of this and the fact that background and the signal are both electron recoils (i.e., NR/ER discrimination is of no value), the requirements on radioactivity in all the surrounding materials of a  $\beta\beta$  TPC are much more stringent than an otherwise similar dark matter detector, unless other background rejection tools are available. However  $\beta\beta$  searches are insensitive to low energy backgrounds (e.g.,  $^{85}\text{Kr}$  and  $^{39}\text{Ar}$ ) important for dark matter.

Very good energy resolution is crucial to avoid background from  $2\nu\beta\beta$  decays and gammas including the prominent 2615 keV line from  $^{208}\text{Tl}$  in the Th chain. Here a combined charge and light measurement largely eliminates the otherwise dominant fluctuations in recombination which lead to anti-correlated fluctuations in charge and light. Because of the high energy of the  $\beta\beta$  signal, charge can be read out directly, and the scintillation measurement is easily tolerant of the dark rates of SiPMs. These goals have led  $\beta\beta$  detectors to have somewhat different optimization than dark matter detectors, although the next generation large Xe dark matter experiments (LZ, XENONnT, DARWIN) have significant  $\beta\beta$  reach.

The recently completed EXO-200 experiment used a single-phase LXe TPC with roughly 110 active kg of Xe enriched to 80.7 %  $^{136}\text{Xe}$  to achieve one of the best  $\beta\beta$  search limits [151]. The energy resolution obtained is (FWHM) of 2.71% (at 2458 keV), and lower values in LXe appear possible. A multi-ton successor experiment, nEXO, has been proposed which would fully cover the inverted neutrino mass hierarchy. [152] EXO-200 featured LAAPDs for light readout, and direct charge readout, while nEXO will use SiPMs.

A related but different approach is to use high pressure gaseous Xe TPC. [153] The lower density requires a large apparatus for given target mass, but has two significant advantages. The larger track size allows the two-electron topology of  $0\nu\beta\beta$  events to be distinguished from single electrons from photoabsorption of background gammas. In addition, the low recombination fraction in the gas phase suppresses recombination fluctuations, allowing higher energy resolution. Recent progress with a 5 kg prototype by the NEXT collaboration has demonstrated the topology based discrimination, and, notably, 1% (FWHM) energy resolution. A  $\sim 100$  kg detector is now under construction, and ton-scale designs being studied. Finally, a long-standing idea that would provide

definitive identification of a  $0\nu\beta\beta$  signal is to extract and tag the ionized Ba daughter via atomic physics techniques [154], either in gas or liquid and gas phases. Significant recent progress by both the EXO and NEXT collaborations has now achieved the key milestone of demonstrating single Ba ion sensitivity in test setups. [155] [156] [157]

### 36.5 Sub-Kelvin detectors

Revised August 2018 by K.D. Irwin (Stanford U.; SLAC).

**Table 36.4:** Some selected experiments using sub-Kelvin equilibrium bolometers to measure the CMB. These experiments constrain the physics of inflation and the absolute mass, hierarchy, and number of neutrino species. The experiment location determines the part of the sky that is observed. The size of the aperture determines the angular resolution. The table also indicates the type of sensor used, the number of sensors, the frequency range, and the number of frequency bands. The number of sensors and frequency range and bands for ongoing upgrades are provided for some experiments in parentheses.

Sub-K CMB Experiment	Location	Aperture	Sensor type	# Sensors (planned)	Frequency (planned)	Bands (planned)
<b>Ground-based</b>						
Atacama Cosmology Telescope (2007–)	Chile	6 m	TES	1,800 (5,334)	90–150 GHz (28–220 GHz)	2 (5)
BICEP/Keck (2006–)	South Pole	26/68 cm	TES	3,200	95–220 GHz	3
CLASS (2015–)	Chile	60 cm	TES	36 (5,108)	40 GHz (40–220 GHz)	1 (4)
POLARBEAR / Simons (2012–)	Chile	3.5 m	TES	1,274 (22,764)	150 GHz (90–220 GHz)	1 (3)
South Pole Telescope (2007–)	South Pole	10 m	TES	1,536 (16,260)	95–150 GHz (95–220 GHz)	2 (3)
<b>Balloon</b>						
EBEX (2013–)	McMurdo	1.5 m	TES	~1,000	150–410 GHz	3
PIPER (2016–)	New Mexico	2 m	TES	5,120	200–600 GHz	4
SPIDER (2014–)	McMurdo	30 cm	TES	1,959	90–280 GHz	3
<b>Satellite</b>						
Planck HFI (2003–)	L2	1.5 m	NTD	52	100–857 GHz	9

Many particle physics experiments utilize detectors operated at temperatures below 1 K. These include WIMP searches, beta-decay experiments to measure the absolute mass of the electron neutrino, and searches for neutrinoless-double-beta decay ( $0\nu\beta\beta$ ) to probe the properties of Majorana neutrinos. Sub-Kelvin detectors also provide important cosmological constraints on particle physics through sensitive measurement of the cosmic microwave background (CMB). CMB measurements probe the physics of inflation at  $\sim 10^{16}$  GeV, and the absolute mass, hierarchy, and number of neutrino species.

Detectors that operate below 1 K benefit from reduced thermal noise and lower material specific heat and thermal conductivity. At these temperatures, superconducting materials, sensors with high responsivity, and cryogenic preamplifiers and multiplexers are available. We provide a simple overview of the techniques and the experiments using sub-K detectors. A useful review of the broad application of low-temperature detectors is provided in [158], and the proceedings of the International Workshop on Low Temperature Detectors [159] provide an overview of the field.

Sub-Kelvin detectors can be categorized as equilibrium thermal detectors or non-equilibrium detectors. Equilibrium detectors measure a temperature rise in a material when energy is deposited. Non-equilibrium detectors are based on the measurement of prompt, non-equilibrated signals and on the excitation of materials with an energy gap.

### 36.5.1 Equilibrium thermal detectors

An equilibrium thermal detector consists of a thermometer and absorber with combined heat capacity  $C$  coupled to a heat bath through a weak thermal conductance  $G$ . The rise time of a thermal detector is limited by the internal equilibration time of the thermometer-absorber system and the electrical time constant of the thermometer. The thermal relaxation time over which heat escapes to the heat bath is  $\tau = C/G$ . Thermal detectors are often designed so that an energy input to the absorber is thermalized and equilibrated through the absorber and thermometer on timescales shorter than  $\tau$ , making the operation particularly simple. An equilibrium thermal detector can be operated as either a calorimeter, which measures an incident energy deposition  $E$ , or as a bolometer, which measures an incident power  $P$ .

In a calorimeter, an energy  $E$  deposited by a particle interaction causes a transient change in the temperature  $\Delta T = E/C$ , where the heat capacity  $C$  can be dominated by the phonons in a lattice, the quasiparticle excitations in a superconductor, or the electronic heat capacity of a metal. The thermodynamic energy fluctuations in the absorber and thermometer have variance

$$\Delta E_{\text{rms}}^2 = k_{\text{B}} T^2 C \quad (36.5)$$

when operated near equilibrium, where  $\Delta E_{\text{rms}}$  is the root-mean-square energy fluctuation,  $k_{\text{B}}$  is the Boltzmann constant and  $T$  is the equilibrium temperature. When a sufficiently sensitive thermometer is used, and the energy is thermalized at frequencies large compared to the thermal response frequency ( $f_{\text{th}} = 1/2\pi\tau$ ), the signal-to-noise ratio is nonzero at frequencies higher than  $f_{\text{th}}$ . In this case, detector energy resolution can be somewhat better than  $\Delta E_{\text{rms}}$  [160]. Deviations from the ideal calorimeter model can cause excess noise and position and energy dependence in the signal shape, leading to degradation in achieved energy resolution.

In a bolometer, a power  $P$  deposited by a stream of particles causes a change in the equilibrium temperature  $\Delta T = P/G$ . The weak thermal conductance  $G$  to the heat bath is usually limited by the flow of heat through a phonon or electron system. The thermodynamic power fluctuations in the absorber and thermometer have power spectral density

$$S_{\text{P}} = NE P^2 = 4k_{\text{B}} T^2 G \quad (36.6)$$

when operated near equilibrium, where the units of NEP (noise equivalent power) are  $\text{W}/\sqrt{\text{Hz}}$ .

The minimization of thermodynamic energy and power fluctuations is a primary motivation for the use of sub-Kelvin thermal detectors. These low temperatures also enable the use of materials and structures with extremely low  $C$  and  $G$ , and the use of superconducting materials and amplifiers.

When very large absorbers are required (e.g. WIMP dark matter searches), dielectric crystals with extremely low specific heat are often used. These materials are operated well below the Debye temperature  $T_{\text{D}}$  of a crystal, where the specific heat scales as  $T^3$ . In this low-temperature limit, the dimensionless phononic heat capacity at fixed volume reduces to

$$\frac{C_{\text{V}}}{N k_{\text{B}}} = \frac{12 \pi^4}{5} \left( \frac{T}{T_{\text{D}}} \right)^3, \quad (36.7)$$

where  $N$  is the number of atoms in the crystal. Normal metals have higher low-temperature specific heat than dielectric crystals, but they also have superior thermalization properties, making them

attractive for some applications in which extreme precision and high energy resolution are required (e.g. beta endpoint experiments to measure neutrino mass using  $^{163}\text{Ho}$ ). At low temperature, the heat capacity of normal metals is dominated by electrons, and is linear in temperature, with convenient form

$$C = \frac{\rho}{A} \gamma VT, \quad (36.8)$$

where  $V$  is the sample volume,  $\gamma$  is the molar specific heat of the material,  $\rho$  is the mass density, and  $A$  is the atomic weight. Superconducting absorbers are also used. Superconductors combine some of the thermalization advantages of normal metals with the lower specific heats associated with insulators when operated well below  $T_c$ , where the electronic heat capacity freezes out, and the material is dominated by phononic heat capacity. At higher temperatures, superconducting materials have more complicated heat capacities, but at their transition temperature  $T_c$ , BCS theory predicts that the electronic heat capacity of a superconductor is  $\sim 2.43$  times the normal metal value.

**Table 36.5:** Selected experiments using sub-Kelvin calorimeters. The table shows only currently operated experiments, and is not exhaustive. WIMP experiments search for dark matter, and beta-decay and neutrinoless double beta decay ( $0\nu\beta\beta$ ) experiments constrain neutrino mass, hierarchy, and Majorana nature. The experiment location determines the characteristics of the radioactive background. The dates of current program phase, detection mode (equilibrium or nonequilibrium phonon measurements, and measurement of ionization or scintillation signals), the absorber and total mass, the sensor type, and the number of sensors and crystals (if different) are given. Many sub-K calorimeter experiments are also in planning and construction phases, including EURECA (dark matter), HOLMES and NuMECs (beta decay), and CUPID-0 ( $0\nu\beta\beta$  decay). Many of the existing experiments are being upgraded to larger mass absorbers, different absorber materials, or lower energy threshold.

Sub-K Calorimeter	Location	Detection mode	Absorber Total mass	Sensor type	# Sensor # Crystal
<b>WIMP</b>					
CRESST II (2003–)	Gran Sasso Italy	Noneq. phon. and scint.	$\text{CaWO}_4$ 5.4 kg	TES	18
EDELWEISS III (2015–)	LSM Modane France	Eq. thermal and ion.	Ge 22 kg	NTD Ge +HEMT	36
SuperCDMS (2012–)	Soudan, USA SNOLAB, Canada	Noneq. phon. and ion.	Ge 9 kg	TES +JFET	120 15
<b>Beta decay</b>					
$\bar{\text{E}}\text{CHo}$ (2012–)	Heidelberg Germany	Eq. thermal	$\text{Au} \cdot ^{163}\text{Ho}$ 0.2 $\mu\text{g}$	MMC	16
<b><math>0\nu\beta\beta</math> decay</b>					
CUORE (2015–)	Gran Sasso Italy	Eq. thermal	$\text{TeO}_2$ 741 kg	NTD Ge	988
AMoRe Pilot (2015–)	Yang Yang S. Korea	Noneq. phon. and scint.	$\text{CaMoO}_4$ 1.5 kg	MMC	5
LUCIFER (2010–)	Gran Sasso Italy	Eq. thermal and scint.	ZnSe 431 g	NTD Ge	1

When very low thermal conductances are required for power measurement (e.g. the measure-

ment of the cosmic microwave background), the weak thermal link is sometimes provided by thin membranes of non-stoichiometric silicon nitride. The thermal conductance of these membranes is:

$$G = 4\sigma AT^3\xi, \quad (36.9)$$

where  $\sigma$  has a value of  $15.7 \text{ mW/cm}^2\text{K}^4$ ,  $A$  is the cross-sectional area perpendicular to the heat flow, and  $\xi$  is a numerical factor with a value of one in the case of specular surface scattering but less than one for diffuse surface scattering. The thermal impedance between the electron and phonon systems can also limit the thermal conductance.

The most commonly used sub-Kelvin thermometer is the superconducting transition-edge sensor (TES) [161]. The TES consists of a superconductor biased at the transition temperature  $T_c$ , in the region between the superconducting and normal state, where its resistance is a strong function of temperature. The TES is voltage biased. The Joule power provides strong negative electrothermal feedback, which improves linearity, speeds up response to faster than  $\tau = C/G$ , and provides tolerance for  $T_c$  variation between multiple TESs in a large array. The current flowing through a TES is read out by a superconducting quantum interference device (SQUID) amplifier. These amplifiers can be cryogenically multiplexed, allowing a large number of TES devices to be read out with a small number of wires to room temperature.

Neutron-transmutation-doped (NTD) germanium and implanted silicon semiconductors read out by cryogenic FET amplifiers are also used as thermometers [160]. Their electrical resistance is exponentially dependent on  $1/T$ , and is determined by phonon-assisted hopping conduction between impurity sites. Finally, the temperature dependence of the permeability of a paramagnetic material is used as a thermometer. Detectors using these thermometers are referred to as metallic magnetic calorimeters (MMC) [162]. These detectors operate without dissipation and are inductively readout by SQUIDs.

Equilibrium thermal detectors are simple, and they have important advantages in precision measurements because of their insensitivity to statistical variations in energy down-conversion pathways, as long as the incident energy equilibrates into an equilibrium thermal distribution that can be measured by a thermometer.

### 36.5.2 Nonequilibrium Detectors

Nonequilibrium detectors use many of the same principles and techniques as equilibrium detectors, but are also sensitive to details of the energy down-conversion before thermalization. Sub-Kelvin nonequilibrium detectors measure athermal phonon signals in a dielectric crystal, electron-hole pairs in a semiconductor crystal, athermal quasiparticle excitations in a superconductor, photon emission from a scintillator, or a combination of two of the above to better discriminate recoils from nuclei or electrons. Because the phonons are athermal, sub-Kelvin nonequilibrium detectors can use absorbers with larger heat capacity, and they use information about the details of energy down-conversion pathways in order to better discriminate signal from background.

In WIMP and neutrino experiments using sub-Kelvin dielectric semiconductors, the recoil energy is typically  $\gtrsim 0.1 \text{ keV}$ . The majority of the energy is deposited in phonons and a minority in ionization and, in some cases, scintillation. The semiconductor bandgap is typically  $\sim \text{eV}$ , and  $k_B T < 10 \text{ } \mu\text{eV}$  at  $T < 1 \text{ K}$ . Thus, high-energy charge pairs and athermal phonons are initially produced. The charge pairs cascade quickly to the gap edge. The high-energy phonons experience isotopic scattering and anharmonic decay, which downshifts the phonon spectrum until the phonon mean free path approaches the characteristic dimension of the absorber. If the crystal is sufficiently pure, these phonons propagate ballistically, preserving information about the interaction location. They are not thermalized, and thus not affected by an increase in the crystal heat capacity, allowing the use of larger absorbers. Sensors similar to those used in sub-K equilibrium thermal detectors

measure the athermal phonons at the crystal surface.

Superconductors can also be used as absorbers in sub-Kelvin detectors when  $T \ll T_c$ . The superconducting gap is typically  $\sim$  meV. Energy absorption breaks Cooper pairs and produces quasiparticles. These particles cascade to the superconducting gap edge, and then recombine after a material-dependent lifetime. During the quasiparticle lifetime, they diffuse through the material. In superconductors with large mean free path, the diffusion length can be more than 1 mm, allowing diffusion to a detector.

In some experiments (e.g. SuperCDMS and CRESST), athermal phonons and quasiparticle diffusion are combined to increase achievable absorber mass. Athermal phonons in a three-dimensional dielectric crystal break Cooper pairs in a two-dimensional superconducting film on the detector surface. The resulting quasiparticles diffuse to thermal sensors (typically a TES) where they are absorbed and detected. While thin superconducting films have diffusion lengths shorter than the diffusion lengths in single crystal superconductors, segmenting the films into small sections and coupling them to multiple TES sensors allows the instrumentation of large absorber volume. The TES sensors can be wired in parallel to combine their output signal.

The combined measurement of the phonon signal and a secondary signal (ionization or scintillation) can provide a powerful discrimination of signal from background events. Nuclear-recoil events in WIMP searches produce proportionally smaller ionization or scintillation signal than electron-scattering events. Since many of the background events are electron recoils, this discrimination provides a powerful veto. Similarly, beta-decay events produce proportionally smaller scintillation signal than alpha-particle events, allowing rejection of alpha backgrounds in neutrino experiments.

Combined phonon and ionization measurement has been implemented in experiments including CDMS I/II, SuperCDMS, and EDELWEISS I/II/III. These experiments use semiconductor crystal absorbers, in which dark-matter scattering events would produce recoiling particles and generate electron-hole pairs and phonons. The electron-hole pairs are separated and drifted to the surface of the crystal by applying an electric field, where they are measured by a JFET or HEMT using similar techniques to those used in 77 K Ge x-ray spectrometers. However, the field strength must be much lower in sub-K detectors to limit the generation of phonon signals by the Neganov-Luke effect, which can confuse the background discrimination. For detectors with very low threshold, the Neganov-Luke effect can also be used to detect generated charge through the induced phonon signal.

Combined phonon and scintillation measurement has been implemented in CRESST II, ROSEBUD, AMoRE and LUCIFER. For example, the CRESST-II experiment uses  $\text{CaWO}_4$  crystal absorbers, and measures both the phonon signal and the scintillation signal with TES calorimeters. A wide variety of scintillating crystals are under consideration, including different tungstates and molybdates,  $\text{BaF}_2$ ,  $\text{ZnSe}$ , and bismuth germanate (BGO).

### 36.6 Low-radioactivity background techniques

Revised November 2019 by A. Piepke (Alabama U.).

The physics reach of low-energy rare-event experiments is often limited by background caused by radioactivity. The problems to be addressed span a wide range of energies, particle types, and interactions. Experiments searching for double beta decay, low energy solar neutrinos or neutrino interactions at nuclear reactors are often concerned about electron recoils and therefore  $\beta$ -decays and  $\gamma$ -ray scattering. The energy scales of interest reach from few keV to few MeV. Dark Matter searches, looking for nuclear recoils, often focus their attention on neutron-induced energy deposits, with electron recoils being of secondary importance. While the energy scales of interest are typically in the keV range, the hadronic physics responsible for the neutron production and interaction spans MeV to GeV. The utilized detector technologies are just as varied, including, among others, large

liquid scintillation detectors, solid state calorimeters, gaseous and liquid tracking detectors and crystal scintillators. Except for reactor bound experiments, these searches are typically performed underground to limit the impact of the cosmic radiation. The depth requirements vary depending on the problem and the chosen detector concept.

Depending on the chosen detector design, the separation of the physics signal from this unwanted interference can be achieved on an event-by-event basis by active event tagging, utilizing some unique event features, or by reducing the flux of the background-creating radiation by appropriate shielding, material selection and surface cleaning. In all cases, the background rate is proportional to the flux of the interfering radiation. Its reduction is, thus, essential for realizing the full physics potential of the experiment. In this context, “low energy” may be defined as the regime of natural, anthropogenic, or cosmogenic radioactivity; all at energies of up to about 10 MeV. See [163] [164] for in-depth reviews of this subject. Following the classification of [163], sources of background may be categorized into the following classes:

1. environmental radioactivity,
2. radio-impurities in detector or shielding components,
3. radon and its progeny,
4. cosmic rays,
5. neutrons from natural fission,  $(\alpha, n)$  reactions and from cosmic-ray muon spallation and capture.

### 36.6.1 Defining the problem

The application defines the requirements. Background goals can be as demanding as a few low-energy events per year in a ton-size detector. The maximal strength of the physics signal of interest can often be estimated theoretically or from limits derived by earlier experiments. The experiments are then designed for the desired signal-to-background ratio. This requires finding the right balance between “clarity of measurement”, ease of construction, schedule and budget.

It is good practice to use detector simulations to translate the background requirements into limits for the radioactivity content of various detector components, requirements for radiation shielding, and allowable cosmic-ray fluxes. This strategy allows the identification of the most critical components early and facilitates the allocation of analysis and development resources in a rational way. The CERN code GEANT4 [165] is a widely used tool for this purpose. It has incorporated sufficient nuclear physics to allow accurate background estimations. Custom-written event generators, modeling *e.g.*, particle correlations in complex decay schemes, deviations from allowed beta spectra or  $\gamma - \gamma$ -angular correlations, are used as well.

### 36.6.2 Environmental radioactivity

The long-lived, naturally occurring radio-nuclides  $^{40}\text{K}$ ,  $^{232}\text{Th}$ , and  $^{238}\text{U}$  have average abundances of 1.6, 11 and 2.7 ppm (corresponding to 412, 45 and 33 Bq/kg, respectively) in the earth’s crust, with large local variations [166]. In most applications,  $\gamma$  radiation emitted in the decay of natural radioactivity and its unstable daughters constitutes the dominant contribution to the local radiation field. Typical low-background applications require levels of natural radioactivity on the order of ppb or ppt in the detector components. Passive or active shielding is used to suppress external  $\gamma$  radiation down to an equivalent level. Fig 36.11 shows the attenuation length  $\lambda(E_\gamma)$  as a function of  $\gamma$ -ray energy  $E_\gamma$  for three common shielding materials: water, copper, lead. Assuming exponential damping, the thickness  $\ell$  required to reduce the external flux by a factor  $f > 1$ , is:

$$\ell = \lambda(E_\gamma) \cdot \ln f . \quad (36.10)$$

At 100 keV, a typical energy scale for dark matter searches (or 2.615 MeV for a typical double-beta decay experiment), attenuation by a factor  $f = 10^5$  requires 67(269) cm of H<sub>2</sub>O, 2.8(34) cm of Cu, or 0.18(23) cm of Pb. Such estimates allow for an order-of-magnitude determination of the experiment dimensions.

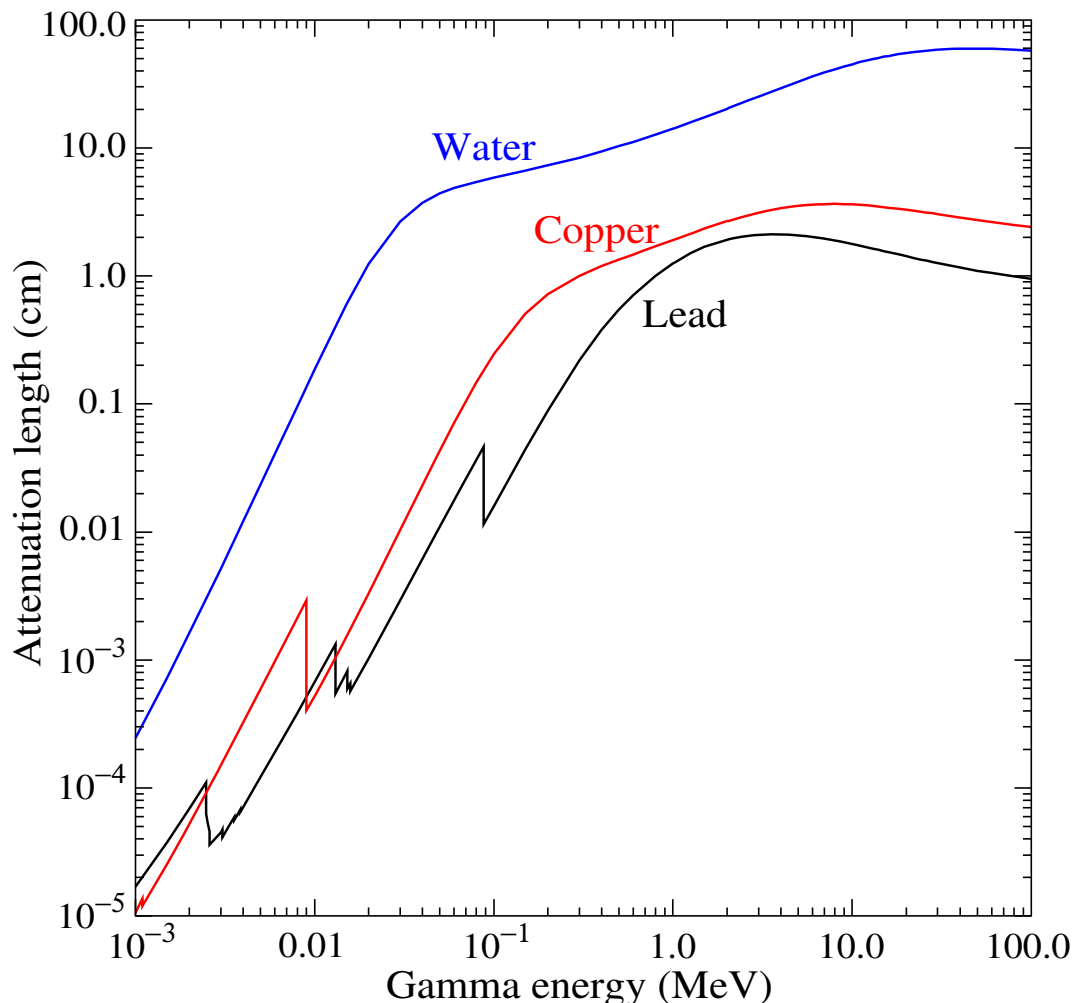


Figure 36.11:  $\gamma$ -ray attenuation lengths in some common shielding materials. The mass attenuation data has been taken from the NIST data base XCOM; see “Atomic Nuclear Properties” at [pdg.lbl.gov](http://pdg.lbl.gov).

As discussed in the following section, shielding materials contain radioactivity too. Consequently, they are chosen such as to contribute as little as possible to the overall background budget. The shielding materials discussed above, when properly selected, fit that requirement. Th/U concentrations in selected H<sub>2</sub>O, Cu and Pb are  $\leq 0.1$  ppt [167],  $\leq 0.5$  ppt [168] and  $\leq 1$  ppt [169], respectively. Although cost effectively available in bulk quantity, steel is often not utilized as it can contain Th/U at concentrations of  $\leq 1$  ppb.

A precise estimation of the the magnitude of the external gamma-ray background, including scattering and the effect of analysis-energy cuts, requires Monte Carlo simulations based on the knowledge of the radioactivity present in the laboratory. Detailed modeling of the  $\gamma$ -ray flux in a large laboratory, or inside the hermetic shielding, needs to cope with a very small probability of generating any signal in the detector. It is often advantageous to calculate the solid angle of the

detector to the background sources and mass attenuation of the radiation shield separately, or to employ importance sampling. The former method can lead to loss of energy-direction correlations while in the latter has to balance CPU-time consumption against the loss of statistical independence. These approaches reduce the computation time required for a statistically meaningful number of detector hits to manageable levels.

Water is commonly used as shielding medium for large detectors. It can be obtained cheaply and purified effectively in large quantity. Water purification technology is commercially available. Ultra-pure water, instrumented with photomultiplier tubes, can serve as active cosmic-ray veto system. Water is also an effective neutron moderator and shield. In more recent underground experiments that involve detectors operating at cryogenic temperature, liquefied gases (e.g. argon) are being used for shielding as well.

### 36.6.3 Radioactive impurities in detector and shielding components

After suppressing the effect of external radioactivity, radioactive impurities, contained in the detector components or attached to their surfaces, become important. Every material contains radioactivity at some level. The activity can be natural, cosmogenic, man-made, or a combination of them. The determination of the activity content of a specific material or component requires case-by-case analyses, and is rarely obtainable from the manufacturer. However, there are some general rules that can be used to guide the pre-selection. For detectors designed to look for electrons (for example in double-beta decay searches or neutrino detection via inverse beta decay or elastic scattering), intrinsic radioactivity is often the principal source of background. For devices detecting nuclear recoils (for example in dark matter searches), this is often of secondary importance as ionization signals can be actively discriminated on an event-by-event basis. In the latter case radioactive decay-induced nuclear reactions, resulting in the emission of energetic neutrons, become a concern. Scattering of these neutrons on the detector material can lead to nuclear-recoil and, thus, background.

For natural radioactivity, a rule of thumb is that refined materials are more radiopure than their source in nature. Substances with high standard reduction potential tend to be cleaner as the refining process preferentially segregates K, Th, and U from electrodeposited materials. For example, Al is often found to contain considerable amounts of Th and U, while electrolytic Cu is very low in primordial activities. K, Th, and U tend to exist as or form compounds with low vapor pressure. Plastics or liquid hydrocarbons, having been refined by distillation, are often quite radiopure. Zone refining utilizes differences in solubility in the liquid and solid phase of the host material to segregate unwanted impurities. This technique is often used in the production of semiconductor detectors. Depending on the material processing, differences in standard reduction potential, boiling point and vapor pressure (for example for U and Ra) may lead to a breakage of decay chain equilibrium. Tabulated radioassay results for a wide range of materials can be found in Refs. [170], [169], [171] and [168]. Radioassay results from previous experiments are being archived at an online database [167].

The long-lived  $^{238}\text{U}$  daughter  $^{210}\text{Pb}$  ( $T_{1/2}=22.3$  y) is found in all shielding lead. It is a background concern at low energies. This is due to the relatively high endpoint energy ( $Q_{\beta}=1.162$  MeV) of its beta-unstable daughter  $^{210}\text{Bi}$ . Lead refined from selected low-U ore typically has specific activities of about 5–30 Bq/kg. For applications that require lower specific activity, ancient lead (for example from Roman ships) is sometimes used. Because the ore processing and lead refining removed most of the  $^{238}\text{U}$ , the  $^{210}\text{Pb}$  decayed during the long waiting time to the level supported by the U-content of the refined lead. Lining the lead with copper to range out the low-energy radiation is another remedy. However, intermediate- $Z$  materials carry additional cosmogenic-activation risks when handled above ground, as will be discussed below.  $^{210}\text{Pb}$  is also found in solders, even lead

free types.

Man-made radioactivity, released during above-ground nuclear testing and nuclear power production, is a source of background. The fission product  $^{137}\text{Cs}$  can often be found attached to the surface of materials. The radioactive noble gas  $^{85}\text{Kr}$ , released into the atmosphere by nuclear reactors and nuclear fuel re-processing, is sometimes a background concern, especially due to its high solubility in organic materials. Post-World War II steel typically contains a few tens of mBq/kg of  $^{60}\text{Co}$ .

Surface activity is not a material property per se but is added during manufacturing and handling. Surface contamination can be effectively removed by clean machining, solvent washing, etching, leaching with dilute acid or their combination. However, different chemical elements for example the decay chain members Ra, Po and Pb have different attachment characteristics and, therefore may react differently to solvents, leading to incomplete cleaning and chain equilibrium breakage. The assembly of low-background detectors is often performed in controlled enclosures (e.g. clean rooms or glove boxes) to avoid contaminating surfaces with environmental substances, such as dust, containing radioactivity at much higher concentrations than the detector components. Due to the small size of dust particles, a fairly large fraction of  $^{226}\text{Ra}$   $\alpha$ -decays results in  $^{222}\text{Rn}$  being ejected into the surrounding gas. This fraction can approach 20% for ultra fine dust. Because of its low reactivity, radon can then spread throughout the detector. When not being processed, components are best stored in sealed bags to limit dust deposition on the surface, even inside clean rooms, and to separate them from radon contained in the air. Nylon bags are also good radon barriers. Storage of parts under vacuum is an alternative solution to limit dust deposition and radon daughter attachment. Surface contamination with environmental dust can be quantified by means of wipe-testing with acid or alcohol wetted Whatman 41 filters. Analysis of acid cleaned paper wipes by means of mass spectroscopy or neutron activation analysis is capable of detecting less than 1 pg/cm<sup>2</sup> of Th and U.

The most demanding low-rate experiments require screening of *all* components for low levels of radioactivity, which can be a time consuming task. The requirements for activity characterization depend on the experiment, the location and amount of a particular component. Monte Carlo simulations are used to quantify these requirements. Sensitivities of the order  $\mu\text{Bq/kg}$  or less are sometimes required for the most critical detector components. At such a level of sensitivity, the characterization becomes a challenging problem in itself. Low-background  $\alpha$ ,  $\beta$ , and  $\gamma$ -ray counting, mass spectroscopy, and neutron activation analysis are commonly used diagnostic techniques.

#### 36.6.4 Radon and its progeny

The noble gas  $^{222}\text{Rn}$ , a pure  $\alpha$ -emitter, is a  $^{238}\text{U}$  decay product. Due to its relatively long half-life of 3.8 d it is released by surface soil and is found in the atmosphere everywhere.  $^{220}\text{Rn}$  (a  $^{232}\text{Th}$  decay product) is unimportant for most low-background experiments because of its short half-life of 55.6 s. It has only very little time to escape from its host material before decaying, with its daughters being immobile. The  $^{222}\text{Rn}$  activity of air ranges from 10 to 100 mBq/L outdoors and 100 to thousands of mBq/L indoors. The natural radon concentration depends on the weather and shows daily and seasonal variations. Radon levels are lowest above the oceans. For electron detectors, it is not the Rn itself that creates background, but its progeny  $^{214}\text{Pb}$ ,  $^{214}\text{Bi}$ ,  $^{210}\text{Bi}$ , which emit energetic beta and  $\gamma$  radiation. Thus, not only the detector itself has to be separated from contact with air, but also air-containing internal voids can be a background concern. Radon is soluble in water and even more so in organic solvents. For large liquid scintillation detectors, radon mobility due to convection and diffusion is a concern. To define a scale: typical double-beta-decay searches are restricted to  $< \mu\text{Bq/kg}_{\text{detector}}$  (or 1 decay per  $\text{kg}_{\text{detector}}$  and per 11.6 days) activities of  $^{222}\text{Rn}$  in the active medium. This corresponds to a steady-state population of 0.5 atoms/ $\text{kg}_{\text{detector}}$ .

The decay of Rn itself is a concern for some recoil type detectors, as nuclear recoil energies in  $\alpha$  decays are substantial (100 keV in the case of  $^{222}\text{Rn}$  decays).

Low-background detectors are often kept sealed from the air and continuously flushed with boil-off nitrogen, which contains only small amounts of Rn. For the most demanding applications, the nitrogen is purified by multiple distillations, or by using pressure swing adsorption chromatography. Then only the Rn outgassing of the piping (due to its intrinsic U content) determines the radon concentration. Radon diffuses readily through thin plastic barriers. If the detector is to be isolated from its environment by means of a membrane, the choice of material is important [172].

Prolonged exposure of detector components or raw materials to air leads to the accumulation of the long-lived radon daughter  $^{210}\text{Pb}$  on surfaces. Due to its low Q-value of 63.5 keV,  $^{210}\text{Pb}$  itself is only a problem when extreme low energy response is important. However, because of its higher Q-value, the lead daughter  $^{210}\text{Bi}$ , is a concern up to the MeV scale. The alpha unstable Bi-daughter  $^{210}\text{Po}$  ( $E_\alpha = 5304$  keV) contributes not only to the alpha background but can also induce the emission of energetic neutrons via ( $\alpha, n$ ) reactions on low-Z materials (such as F, C, Si...etc). The neutrons, in turn, may capture on other detector components, creating energetic background. The ( $\alpha, n$ ) reaction yield induced by the  $\alpha$  decay of  $^{210}\text{Po}$  is typically small (about  $6 \cdot 10^{-6} n/\alpha$  in Teflon, for example). This creates a memory effect, the air exposure history impacts the ( $\alpha, n$ ) background component.

Some data is available on the deposition of radon daughters from air onto materials, see e.g. [173], [174] and [175]. This data indicates a large spread of effective radon daughter collection distances ranging from a few *cm* to a few *m* in air. This large spread may indicate dependence on hidden, uncontrolled variables. These considerations limit the allowable air exposure time but only within a wide range. Many experiments therefore adopt to perform the assembly of detector components in a radon-reduced atmosphere to counter this uncertainty.

In case raw materials (e.g. in the form of granules) were exposed to air at the production site, the bulk (instead of the surface as discussed before) of the finished detector components may be loaded with  $^{210}\text{Pb}$  and its daughters. These are difficult to detect as no energetic gamma radiation is emitted in their decays. Careful air-exposure management is the only way to reduce this source of background. This can be achieved by storing the parts under a protective low-radon cover gas or keeping them sealed from radon.

State-of-the-art detectors can detect radon outgassing even at the level of few atoms. Solid state, scintillation, or gas detectors utilize alpha spectroscopy or are exploiting the fast  $\beta - \alpha$  decay sequences of  $^{214}\text{Bi}$  and  $^{214}\text{Po}$ . The efficiency of these devices is sometimes boosted by electrostatic collection of radon ions from a large gas volume onto a small detector. Cryogenic radon collection can also boost the radon sensitivity. Radon outgassing measurement campaigns, similar to the radioactivity measurements discussed above, are conducted by collaborations to assure that the internal radon production stays within its allowance.

### 36.6.5 *Cosmic rays*

Cosmic radiation, discussed in detail in Chapter 30, is a source of background for just about any non-accelerator experiment. Primary cosmic rays are about 90% protons, 9% alpha particles, and the rest heavier nuclei (Fig 30.1). They are totally attenuated within the first few  $\text{hg}/\text{cm}^2$  of atmospheric thickness. At sea level secondary particles ( $\pi^\pm : p : e^\pm : n : \mu^\pm$ ) are observed with relative intensities 1 : 13 : 340 : 480 : 1420 ( [176]; also see Fig 30.3).

All but the muon and the neutron components are readily absorbed by overburden such as building ceilings and passive shielding. Only if there is very little overburden ( $\lesssim 10 \text{ g}/\text{cm}^2$  [163]) do pions and protons need to be considered when estimating the production rate of cosmogenic radioactivity.

Sensitive experiments are, thus, operated deep underground where essentially only muons can penetrate. As shown in Fig-30.7, the muon intensity falls off rapidly with depth. Active detection systems, capable of tagging events correlated in time with cosmic-ray activity, are needed, depending on the overburden.

The muonic background is related to low-radioactivity techniques insofar as photo-nuclear interactions with atomic nuclei can produce long-lived radioactivity directly or indirectly via the creation of neutrons. This happens at any overburden, however, at strongly depth dependent rates. Muon bremsstrahlung, created in high- $Z$  shielding materials, contributes to the low energy background too. Active muon detection systems are effective in reducing cosmogenic background, but only for activities with sufficiently short half-lives, allowing vetoing with reasonable detector dead time.

Cosmogenic activation of detector components at the surface can be an issue for low-background experiments. Proper management of parts and materials above ground during manufacturing and detector assembly minimizes the accumulation of long-lived activity. Cosmogenic activation is most important for intermediate- $Z$  materials such as Cu and Fe. For the most demanding applications, metals are stored and transported under sufficient shielding to stop the hadronic component of the cosmic rays. Parts can be stored underground for long periods before being used. Underground machine shops are sometimes used to limit the duration of exposure at the surface. Some experiments are even electro-forming copper underground.

### 36.6.6 *Neutrons*

Neutrons contribute to the background of low-energy experiments in different ways: directly through nuclear recoil in the detector medium, and indirectly, through the production of radio-nuclides, capture  $\gamma$ s and inelastic scattering inside the detector and its components. The indirect mechanisms allow even remote materials to contribute to the background by means of penetrating  $\gamma$  radiation. Neutrons are thus an important source of low-energy background. They are produced in different ways:

1. At the earth's surface the flux of cosmic-ray secondary neutrons is exceeded only by that of muons;
2. Energetic tertiary neutrons are produced by cosmic-ray muons by nuclear spallation in the detector and laboratory walls;
3. In high- $Z$  materials, often used in radiation shields, nuclear capture of negative muons results in the emission of neutrons;
4. Natural radioactivity has a neutron component through spontaneous fission and  $(\alpha, n)$ -reactions.

A calculation with the hadronic simulation code FLUKA [177], using the known energy distribution of secondary neutrons at the earth's surface [178], yields a mass attenuation of 1.5 hg/cm<sup>2</sup> in concrete for secondary neutrons. In case energy-dependent neutron-capture cross sections are known, such calculations can be used to obtain the production rate of particular radio-nuclides.

At an overburden of only few meters water equivalent, neutron production by muons becomes the dominant mechanism. Neutron production rates are high in high- $Z$  shielding materials. A high- $Z$  radiation shield, discussed earlier as being effective in reducing background due to external radioactivity, thus acts as a source for cosmogenic tertiary high-energy neutrons. Depending on the overburden and the radioactivity content of the laboratory, there is an optimal shielding thickness. Water shields, although bulky, are an attractive alternative due to their low neutron production yield and self-shielding.

Shields made from plastic or water are commonly used to reduce the neutron flux. The shield is sometimes doped with a substance having a high thermal neutron capture cross section (such as

boron) to absorb thermal neutrons more quickly. The hydrogen, contained in these shields, serves as a target for elastic scattering, and is effective in reducing the neutron energy. Neutrons from natural radioactivity have relatively low energies and can be effectively suppressed by a neutron shield. Ideally, such a neutron shield should be inside the lead to be effective for tertiary neutrons. However, this is rarely done as it increases the neutron production target (in form of the passive shield), and the costs increase as the cube of the linear dimensions. An active cosmic-ray veto is an effective solution, correlating a neutron with its parent muon. This solution works best if the veto system is as far away from the detector as feasible (outside the radiation shield) in order to correlate as many background-producing muons with neutrons as possible. The vetoed time after a muon hit needs to be sufficiently long to assure muon bremsstrahlung and neutron-induced backgrounds are sufficiently suppressed. An upper limit to the allowable veto period is given by the veto-induced deadtime, which is related to the muon hit rate on the veto detector. This consideration also constitutes the limiting factor for the physical size of the veto system (besides the cost). The background caused by neutron-induced radioactivity with live-times far exceeding the veto time cannot be addressed in this way. Moving the detector deep underground, and thus reducing the muon flux, is the only technique that addresses all sources of cosmogenic the neutron background.

### References

- [1] R. M. Baltrusaitis *et al.*, Nucl. Instrum. Meth. **A240**, 410 (1985).
- [2] D. J. Bird *et al.* (HiRes), Astrophys. J. **424**, 491 (1994).
- [3] T. Abu-Zayyad *et al.*, Nucl. Instrum. Meth. **A450**, 253 (2000).
- [4] H. Tokuno *et al.*, Nucl. Instrum. Meth. **A676**, 54 (2012), [[arXiv:1201.0002](#)].
- [5] J. Abraham *et al.* (Pierre Auger), Nucl. Instrum. Meth. **A620**, 227 (2010), [[arXiv:0907.4282](#)].
- [6] R. Mussa and G. Ciaccio (Pierre Auger), Eur. Phys. J. Plus **127**, 94 (2012).
- [7] T. Fujii *et al.*, Astropart. Phys. **74**, 64 (2016), [[arXiv:1504.00692](#)].
- [8] F. Arqueros, J. R. Hoerandel and B. Keilhauer, Nucl. Instrum. Meth. **A597**, 23 (2008), [[arXiv:0807.3844](#)].
- [9] F. Arqueros, J. R. Hoerandel and B. Keilhauer, Nucl. Instrum. Meth. **A597**, 1 (2008), [[arXiv:0807.3760](#)].
- [10] J. Rosado, F. Blanco and F. Arqueros, Astropart. Phys. **34**, 164 (2010), [[arXiv:1004.3971](#)].
- [11] M. Ave *et al.* (AIRFLY), Astropart. Phys. **28**, 41 (2007), [[arXiv:astro-ph/0703132](#)].
- [12] J. Rosado, F. Blanco and F. Arqueros, Astropart. Phys. **55**, 51 (2014), [[arXiv:1401.4310](#)].
- [13] J. H. Boyer *et al.*, Nucl. Instrum. Meth. **A482**, 457 (2002).
- [14] J. T. Brack *et al.*, Astropart. Phys. **20**, 653 (2004).
- [15] B. Fick *et al.*, JINST **1**, 11, P11003 (2006).
- [16] J. Abraham *et al.* (Pierre Auger), Astropart. Phys. **33**, 108 (2010), [[arXiv:1002.0366](#)].
- [17] P. Abreu *et al.* (Pierre Auger), Astropart. Phys. **34**, 368 (2011), [[arXiv:1010.6162](#)].
- [18] R. Thalman *et al.* Journal of Quantitative Spectroscopy and Radiative Transfer , **147**, 171 (2014), Erratum-ibid. **189**, 281 (2017).
- [19] J. Abraham *et al.* [Pierre Auger Collab.], Nucl. Instrum. Methods **A789**, 172 (2015).
- [20] M. Unger *et al.*, Nucl. Instrum. Meth. **A588**, 433 (2008), [[arXiv:0801.4309](#)].
- [21] T.K. Gaisser and A.M. Hillas, *Proc. 15th Int. Cosmic Ray Conf.* Bulgarska Akademiia na Naukite, Conf. Papers **8**, 353 (1978), (archived at <http://adsabs.harvard.edu/abs/1977ICRC....8..353G>).

- [22] A. Huang, G. Medina-Tanco and A. Santangelo, *Experimental Astronomy* **40**, 1 (2015).
- [23] P. A. Klimov *et al.*, *Space Sci. Rev.* **212**, 3-4, 1687 (2017), [[arXiv:1706.04976](#)].
- [24] G. Abdellaoui *et al.* (JEM-EUSO), *Journal of Instrumentation* **13**, 5 (2018), ISSN 17480221.
- [25] L. Wiencke and A. Olinto (JEM-EUSO), *PoS ICRC2017*, 1097 (2018).
- [26] F. Capel *et al.*, *Advances in Space Research* **62**, 2954 (2018).
- [27] A. V. Olinto *et al.*, *PoS ICRC2017*, 542 (2018), [35,542(2017)], [[arXiv:1708.07599](#)].
- [28] J. Holder *et al.*, *AIP Conf. Proc.* **1085**, 657 (2009), [[arXiv:0810.0474](#)].
- [29] F. Aharonian *et al.* (H.E.S.S.), *Astron. Astrophys.* **457**, 899 (2006), [[arXiv:astro-ph/0607333](#)].
- [30] J. Albert *et al.* (MAGIC), *Astrophys. J.* **674**, 1037 (2008), [[arXiv:0705.3244](#)].
- [31] T. C. Weekes *et al.*, *Astrophys. J.* **342**, 379 (1989).
- [32] A. M. Hillas *et al.*, *Astrophys. J.* **503**, 744 (1998).
- [33] <http://tevcat.uchicago.edu/>.
- [34] F. Aharonian *et al.* (H.E.S.S.), *Astrophys. J.* **636**, 777 (2006), [[arXiv:astro-ph/0510397](#)].
- [35] M. de Naurois and D. Mazin, *Comptes Rendus Physique* **16**, 610 (2015), [[arXiv:1511.00463](#)].
- [36] N. Park, *PoS ICRC2017*, [arXiv:1808.10495](#) (2018), [[arXiv:1808.10495](#)].
- [37] A. M. Hillas, *Astropart. Phys.* **43**, 19 (2013).
- [38] B. S. Acharya *et al.* (CTA Consortium), *Astropart. Phys.* **43**, 3 (2013).
- [39] A. Bernstein *et al.*, *Report on the Depth Requirements for a Massive Detector at Homestake* (2009), [[arXiv:0907.4183](#)].
- [40] Y. Ashie *et al.* (Super-Kamiokande), *Phys. Rev.* **D71**, 112005 (2005), [[hep-ex/0501064](#)].
- [41] S. Kasuga *et al.*, *Phys. Lett.* **B374**, 238 (1996).
- [42] M. Shiozawa (Super-Kamiokande), *Nucl. Instrum. Meth.* **A433**, 240 (1999).
- [43] K. Abe *et al.* (Super-Kamiokande), *Phys. Rev.* **D83**, 052010 (2011), [[arXiv:1010.0118](#)].
- [44] J. F. Beacom and M. R. Vagins, *Phys. Rev. Lett.* **93**, 171101 (2004), [[hep-ph/0309300](#)].
- [45] J. Boger *et al.* (SNO), *Nucl. Instrum. Meth.* **A449**, 172 (2000), [[arXiv:nucl-ex/9910016](#)].
- [46] T. K. Gaisser, F. Halzen and T. Stanev, *Phys. Rept.* **258**, 173 (1995), [Erratum: *Phys. Rept.*271,355(1996)], [[hep-ph/9410384](#)].
- [47] J.G. Learned and K. Mannheim, *Ann. Rev. Nucl. and Part. Sci.* **50**, 679 (2000).
- [48] U. F. Katz and C. Spiering, *Prog. Part. Nucl. Phys.* **67**, 651 (2012), [[arXiv:1111.0507](#)].
- [49] M. G. Aartsen *et al.* (IceCube), *J. Phys.* **G44**, 5, 054006 (2017), [[arXiv:1607.02671](#)].
- [50] S. Adrián-Martínez *et al.* (KM3NeT), *J. Phys.* **G43**, 8, 084001 (2016), [[arXiv:1601.07459](#)].
- [51] A. D. Avrorin *et al.*, *Phys. Part. Nucl.* **46**, 2, 211 (2015).
- [52] M. G. Aartsen *et al.* (IceCube) (2014), [[arXiv:1412.5106](#)].
- [53] S. Adrián-Martínez *et al.* (KM3NeT), *Eur. Phys. J.* **C74**, 9, 3056 (2014), [[arXiv:1405.0839](#)].
- [54] A. V. Akindinov *et al.*, *Eur. Phys. J.* **C79**, 9, 758 (2019), [[arXiv:1902.06083](#)].
- [55] C. Kopper (for the IceCube Collab.), contribution to ICRC2017.
- [56] M. G. Aartsen *et al.* (IceCube), *Phys. Rev. Lett.* **113**, 101101 (2014), [[arXiv:1405.5303](#)].
- [57] A. Albert *et al.* (ANTARES), *Astrophys. J.* **853**, 1, L7 (2018), [[arXiv:1711.07212](#)].
- [58] M. G. Aartsen *et al.* (IceCube), *Phys. Rev.* **D91**, 7, 072004 (2015), [[arXiv:1410.7227](#)].

- [59] M. G. Aartsen *et al.* (IceCube, Fermi-LAT, MAGIC, AGILE, ASAS-SN, HAWC, H.E.S.S., INTEGRAL, Kanata, Kiso, Kapteyn, Liverpool Telescope, Subaru, Swift NuSTAR, VERITAS, VLA/17B-403), *Science* **361**, 6398, eaat1378 (2018), [[arXiv:1807.08816](#)].
- [60] M. G. Aartsen *et al.* (IceCube), *Science* **361**, 6398, 147 (2018), [[arXiv:1807.08794](#)].
- [61] G. Illuminati (for the ANTARES and IceCube Collabs.), contribution to ICRC2019.
- [62] M. G. Aartsen *et al.* (IceCube), *Phys. Rev.* **D99**, 3, 032007 (2019), [[arXiv:1901.05366](#)].
- [63] D. Williams (for the IceCube Collab.), contribution to ICRC2019.
- [64] R. Coniglione (for the ANTARES and KM3NeT Collabs.), contribution to ICRC2019.
- [65] K. Greisen, *Phys. Rev. Lett.* **16**, 748 (1966).
- [66] G. T. Zatsepin and V. A. Kuzmin, *JETP Lett.* **4**, 78 (1966), [*Pisma Zh. Eksp. Teor. Fiz.*4,114(1966)].
- [67] R. Abbasi *et al.* (IceCube), *Astropart. Phys.* **34**, 382 (2011), [[arXiv:1004.1694](#)].
- [68] S. R. Klein, *Nucl. Phys. Proc. Supl.* **229-232**, 284 (2012), [[arXiv:1012.1407](#)].
- [69] G. A. Askar'yan, *Sov. Phys. JETP* **14**, 2, 441 (1962), [*Zh. Eksp. Teor. Fiz.*41,616(1961)].
- [70] G.A. Askaryan, *Sov. Phys. JETP* **21**, 658 (1965).
- [71] C. W. James *et al.*, *Phys. Rev.* **E84**, 056602 (2011), [[arXiv:1007.4146](#)].
- [72] J. Alvarez-Muniz, R. A. Vazquez and E. Zas, *Phys. Rev.* **D62**, 063001 (2000), [[arXiv:astro-ph/0003315](#)].
- [73] C. Glaser *et al.* (2019), [[arXiv:1906.01670](#)].
- [74] D. Saltzberg *et al.*, *Phys. Rev. Lett.* **86**, 2802 (2001), [[hep-ex/0011001](#)].
- [75] O. Scholten *et al.*, *J. Phys. Conf. Ser.* **81**, 012004 (2007).
- [76] A. G. Vieregge, K. Bechtol and A. Romero-Wolf, *JCAP* **1602**, 02, 005 (2016), [[arXiv:1504.08006](#)].
- [77] L. Gerhardt and S. R. Klein, *Phys. Rev.* **D82**, 074017 (2010), [[arXiv:1007.0039](#)].
- [78] J. Alvarez-Muniz, R. A. Vazquez and E. Zas, *Phys. Rev.* **D61**, 023001 (2000), [[arXiv:astro-ph/9901278](#)].
- [79] M. G. Aartsen *et al.* (IceCube), *Phys. Rev.* **D98**, 6, 062003 (2018), [[arXiv:1807.01820](#)].
- [80] A. Aab *et al.* (Pierre Auger), *JCAP* **1910**, 10, 022 (2019), [[arXiv:1906.07422](#)].
- [81] J. D. Bray *et al.*, *Phys. Rev.* **D91**, 6, 063002 (2015), [[arXiv:1502.03313](#)].
- [82] O. Scholten *et al.*, *Phys. Rev. Lett.* **103**, 191301 (2009), [[arXiv:0910.4745](#)].
- [83] P. W. Gorham *et al.* (ANITA), *Phys. Rev.* **D99**, 12, 122001 (2019), [[arXiv:1902.04005](#)].
- [84] P. Allison *et al.* (ARA), in “36th International Cosmic Ray Conference (ICRC 2019) Madison, Wisconsin, USA, July 24-August 1, 2019,” (2019), [[arXiv:1907.11125](#)].
- [85] A. Anker *et al.* (2019), [[arXiv:1909.00840](#)].
- [86] T. Winchen *et al.*, *J. Phys. Conf. Ser.* **1181**, 1, 012077 (2019), [[arXiv:1903.08472](#)].
- [87] J. Stettner (IceCube), in “HAWC Contributions to the 36th International Cosmic Ray Conference (ICRC2019),” (2019), [[arXiv:1908.09551](#)].
- [88] A. van Vliet, J. R. Horandel and R. Alves Batista, *PoS ICRC2017*, 562 (2018), [[35,562\(2017\)](#)], [[arXiv:1707.04511](#)].
- [89] J. A. Aguilar *et al.* (2019), [[arXiv:1907.12526](#)].
- [90] J. G. Learned and S. Pakvasa, *Astropart. Phys.* **3**, 267 (1995), [[hep-ph/9405296](#)].

- [91] J. L. Feng *et al.*, Phys. Rev. Lett. **88**, 161102 (2002), [[hep-ph/0105067](#)].
- [92] P. W. Gorham *et al.* (ANITA), Phys. Rev. Lett. **121**, 16, 161102 (2018), [[arXiv:1803.05088](#)].
- [93] J. Álvarez Muñiz *et al.* (GRAND), Sci. China Phys. Mech. Astron. **63**, 1, 219501 (2020), [[arXiv:1810.09994](#)].
- [94] M. Detrixhe *et al.* (ANITA-II), Phys. Rev. **D83**, 023513 (2011), [[arXiv:1008.1282](#)].
- [95] R.D. Dagkesamanskii and I.M. Zheleznykh, Sov. Phys. JETP Lett. **50**, 233 (1989).
- [96] C. W. James *et al.*, EPJ Web Conf. **135**, 04001 (2017), [[arXiv:1704.05336](#)].
- [97] J. D. Bray, Astropart. Phys. **77**, 1 (2016), [[arXiv:1601.02980](#)].
- [98] J.A. Dowdeswell and S. Evans, Rept. on Prog. in Phys. **67**, 1821 (2004).
- [99] P. Allison *et al.*, Astropart. Phys. **108**, 63 (2019), [[arXiv:1712.03301](#)].
- [100] A. Anker *et al.*, JCAP **1911**, 030 (2019), [[arXiv:1909.02677](#)].
- [101] S. W. Barwick *et al.*, JCAP **1807**, 07, 055 (2018), [[arXiv:1804.10430](#)].
- [102] C. Deaconu *et al.*, Phys. Rev. **D98**, 4, 043010 (2018), [[arXiv:1805.12576](#)].
- [103] P. W. Gorham *et al.* (ANITA), Phys. Rev. Lett. **103**, 051103 (2009), [[arXiv:0812.2715](#)].
- [104] I. Kravchenko *et al.*, Phys. Rev. **D73**, 082002 (2006), [[arXiv:astro-ph/0601148](#)].
- [105] P. Allison *et al.* (ARA), Phys. Rev. **D93**, 8, 082003 (2016), [[arXiv:1507.08991](#)].
- [106] J. Avva *et al.*, Nucl. Instrum. Meth. **A869**, 46 (2017), [[arXiv:1605.03525](#)].
- [107] A. Anker *et al.* (ARIANNA), Adv. Space Res. **64**, 2595 (2019), [[arXiv:1903.01609](#)].
- [108] F. G. Schroder, Prog. Part. Nucl. Phys. **93**, 1 (2017), [[arXiv:1607.08781](#)].
- [109] T. Huege, Braz. J. Phys. **44**, 520 (2014), [,1294(2013)], [[arXiv:1310.6927](#)].
- [110] S. Buitink *et al.*, Phys. Rev. **D90**, 8, 082003 (2014), [[arXiv:1408.7001](#)].
- [111] T. Huege, Phys. Rept. **620**, 1 (2016), [[arXiv:1601.07426](#)].
- [112] S. W. Barwick *et al.*, Astropart. Phys. **90**, 50 (2017), [[arXiv:1612.04473](#)].
- [113] A. Balagopal V. *et al.*, Eur. Phys. J. **C78**, 2, 111 (2018), [erratum: Eur. Phys. J. **C78**, 1017 (2018)], [[arXiv:1712.09042](#)].
- [114] A. Aab *et al.* (Pierre Auger), Phys. Rev. Lett. **116**, 24, 241101 (2016), [[arXiv:1605.02564](#)].
- [115] P. A. Bezyazeev *et al.*, Phys. Rev. **D97**, 12, 122004 (2018), [[arXiv:1803.06862](#)].
- [116] W. D. Apel *et al.* (LOPES), Phys. Rev. **D90**, 6, 062001 (2014), [[arXiv:1408.2346](#)].
- [117] D. R. Nygren, in “Proceedings, 1975 PEP Summer Study, Berkeley, July 28-August 20, 1975,” 126–133 (1975).
- [118] L. S. Miller, S. Howe and W. E. Spear, Phys. Rev. **166**, 871 (1968), URL <https://link.aps.org/doi/10.1103/PhysRev.166.871>.
- [119] E. Aprile and T. Doke, Rev. Mod. Phys. **82**, 2053 (2010), [[arXiv:0910.4956](#)].
- [120] V. Chepel and H. Araujo, JINST **8**, R04001 (2013), [[arXiv:1207.2292](#)].
- [121] D. Gonzalez-Diaz, F. Monrabal and S. Murphy, Nucl. Instrum. Meth. **A878**, 200 (2018), [[arXiv:1710.01018](#)].
- [122] J. J. Gomez-Cadenas, F. Monrabal Capilla and P. Ferrario, Front.in Phys. **7**, 51 (2019), [[arXiv:1903.02435](#)].
- [123] H. J. Maris, Journal of the Physical Society of Japan **77**, 11, 111008 (2008), URL <https://doi.org/10.1143/JPSJ.77.111008>.

- [124] L. Bruschi, G. Mazzi and M. Santini, Phys. Rev. Lett. **28**, 1504 (1972), URL <https://link.aps.org/doi/10.1103/PhysRevLett.28.1504>.
- [125] E. Aprile *et al.*, Nature **568**, 7753, 532 (2019), URL <https://doi.org/10.1038/s41586-019-1124-4>.
- [126] K. Winger *et al.*, Journal of Environmental Radioactivity **80**, 2, 183 (2005), ISSN 0265-931X, URL <http://www.sciencedirect.com/science/article/pii/S0265931X04002887>.
- [127] H. Loosli, Earth and Planetary Science Letters **63**, 1, 51 (1983), ISSN 0012-821X, URL <http://www.sciencedirect.com/science/article/pii/0012821X83900213>.
- [128] E. Aprile *et al.* (XENON), Eur. Phys. J. **C75**, 11, 546 (2015), [arXiv:1503.07698].
- [129] M. Schumann, J. Phys. **G46**, 10, 103003 (2019), [arXiv:1903.03026].
- [130] E. Aprile *et al.*, JINST **9**, 11, P11012 (2014), [arXiv:1408.6206].
- [131] F. Neves *et al.*, JINST **12**, 01, P01017 (2017), [arXiv:1612.07965].
- [132] D. S. Akerib *et al.* (LUX Collaboration), Phys. Rev. D **97**, 102008 (2018), URL <https://link.aps.org/doi/10.1103/PhysRevD.97.102008>.
- [133] D. S. Akerib *et al.* (LUX), Phys. Rev. **D95**, 1, 012008 (2017), [arXiv:1610.02076].
- [134] M. Szydagis *et al.*, Journal of Instrumentation **6**, 10, P10002 (2011), URL <https://doi.org/10.1088%2F1748-0221%2F6%2F10%2Fp10002>.
- [135] M. Kimura *et al.*, Phys. Rev. **D100**, 3, 032002 (2019), [arXiv:1902.01501].
- [136] R. Ajaj *et al.* (DEAP), Phys. Rev. **D100**, 2, 022004 (2019), [arXiv:1902.04048].
- [137] P. Agnes *et al.* (DarkSide), Phys. Rev. **D93**, 8, 081101 (2016), [Addendum: Phys. Rev. D95, no.6, 069901(2017)], [arXiv:1510.00702].
- [138] E. Aprile *et al.* (XENON), Phys. Rev. Lett. **119**, 18, 181301 (2017), [arXiv:1705.06655].
- [139] X. Cui *et al.* (PandaX-II), Phys. Rev. Lett. **119**, 18, 181302 (2017), [arXiv:1708.06917].
- [140] D. S. Akerib *et al.*, Phys. Rev. Lett. **118**, 25, 251302 (2017).
- [141] D. S. Akerib *et al.* (LUX-ZEPLIN) (2018), [arXiv:1802.06039].
- [142] E. Aprile *et al.* (XENON), JCAP **1604**, 04, 027 (2016), [arXiv:1512.07501].
- [143] H. Zhang *et al.* (PandaX), Sci. China Phys. Mech. Astron. **62**, 3, 31011 (2019), [arXiv:1806.02229].
- [144] C. E. Aalseth *et al.*, Eur. Phys. J. Plus **133**, 131 (2018), [arXiv:1707.08145].
- [145] J. Aalbers *et al.*, Journal of Cosmology and Astroparticle Physics **2016**, 11, 017 (2016), URL <https://doi.org/10.1088%2F1475-7516%2F2016%2F11%2F017>.
- [146] W. Guo and D. N. McKinsey, Phys. Rev. **D87**, 11, 115001 (2013), [arXiv:1302.0534].
- [147] D. R. Nygren, J. Phys. Conf. Ser. **460**, 012006 (2013).
- [148] C. A. J. O'Hare *et al.*, Phys. Rev. **D92**, 6, 063518 (2015), [arXiv:1505.08061].
- [149] S. M. Bilenky and C. Giunti, Mod. Phys. Lett. **A27**, 1230015 (2012), [arXiv:1203.5250].
- [150] S. R. Elliott, A. A. Hahn and M. K. Moe, Phys. Rev. Lett. **59**, 2020 (1987), URL <http://link.aps.org/doi/10.1103/PhysRevLett.59.2020>.
- [151] G. Anton *et al.* (EXO-200), Phys. Rev. Lett. **123**, 16, 161802 (2019), [arXiv:1906.02723].
- [152] S. A. Kharusi *et al.* (nEXO) (2018), [arXiv:1805.11142].
- [153] D. Nygren, Nucl. Instrum. Meth. **A603**, 337 (2009).
- [154] M. K. Moe, Phys. Rev. **C44**, 931 (1991), [1019(1991)].

- [155] A. D. McDonald *et al.*, Phys. Rev. Lett. **120**, 13, 132504 (2018), [[arXiv:1711.04782](#)].
- [156] C. Chambers *et al.* (nEXO), Nature **569**, 7755, 203 (2019), [[arXiv:1806.10694](#)].
- [157] P. Thapa *et al.* (2019), [[arXiv:1904.05901](#)].
- [158] C. Enss, editor, *Cryogenic particle detection*, volume 99 of *Topics in applied physics*, Springer, Berlin, Germany (2005).
- [159] E. Shirokoff (ed.), *Proc. 15th Int. Workshop on Low Temperature Detectors (LTD-15)*, J. Low Temp. Phys. **176**, 131–1108 (2014).
- [160] S.H. Moseley, J.C. Mather, and D. McCammon, J. Appl. Phys. **56**, 1257 (1984).
- [161] K.D. Irwin, Appl. Phys. Lett. **66**, 1998 (1995).
- [162] S.R. Bandler *et al.*, J. Low. Temp. Phys. **93**, 709 (1993).
- [163] G. Heusser, Ann. Rev. Nucl. Part. Sci. **45**, 543 (1995).
- [164] J. A. Formaggio and C. J. Martoff, Ann. Rev. Nucl. Part. Sci. **54**, 361 (2004).
- [165] S. Agostinelli *et al.* (GEANT4), Nucl. Instrum. Meth. **A506**, 250 (2003).
- [166] U. N. S. C. on the Effects of Atomic Radiation, *Sources and Effects of Ionizing Radiation, p233*, United Nations (2010).
- [167] <http://www.radiopurity.org>.
- [168] N. Abgrall *et al.*, Nucl. Instrum. Meth. **A828**, 22 (2016), [[arXiv:1601.03779](#)].
- [169] D. S. Leonard *et al.*, Nucl. Instrum. Meth. **A591**, 490 (2008), [[arXiv:0709.4524](#)].
- [170] J. Jagam and J. Simpson, Nucl. Instrum. Meth. **A324**, 389 (1993).
- [171] D. S. Leonard *et al.*, Nucl. Instrum. Meth. **A871**, 169 (2017), [[arXiv:1703.10799](#)].
- [172] M. Wojcik *et al.*, Nucl. Instrum. Meth. **A449**, 158 (2000).
- [173] V. E. Guiseppe *et al.*, AIP Conf. Proc. **1338**, 95 (2011), [[arXiv:1101.0126](#)].
- [174] M. Stein *et al.*, Nucl. Instrum. Meth. **A880**, 92 (2018), [[arXiv:1708.09476](#)].
- [175] E. S. Morrison *et al.*, AIP Conf. Proc. **1921**, 1, 090002 (2018), [[arXiv:1708.08534](#)].
- [176] National Council on Radiation Protection and Measurement, Report 94, Bethesda, MD (1987).
- [177] T. Boehlen *et al.*, Nuclear Data Sheets **120**, 211 (2014), <http://www.fluka.org/fluka.php>.
- [178] M.S. Gordon *et al.*, IEEE Trans. **NS51**, 3427 (2004).